Markus Stütz, BSc

Surface Structuring of Biodegradable Mg-alloys by Electron Beam Technique

Master's Thesis

to obtain the academic degree of

Diplom-Ingenieur (Master of Science)

Master Program of Mechanical Engineering

Submitted at

Graz University of Technology

Supervision

Dipl.-Ing. Dr.techn. Fernando Gustavo Warchomicka
Ass.Prof. Dr.techn. María Cecilia Poletti

Institute for Materials Science and Welding
Head: Univ.-Prof. Dipl.-Ing. Dr.techn. Priv.-Doz. Christof Sommitsch

Graz, May 2014

Eidesstattliche Erklärung

Affidavit

Ich erkläre an Eides statt, dass ich die vorliegende Arbeit selbstständig verfasst, andere als die angegebenen Quellen/Hilfsmittel nicht benutzt, und die den benutzten Quellen wörtlich und inhaltlich entnommenen Stellen als solche kenntlich gemacht habe. Das in TUGRAZonline hochgeladene Textdokument ist mit der vorliegenden Masterarbeit identisch.

I declare that I have authored this thesis independently, that I have not used other than the declared sources/resources, and that I have explicitly indicated all material which has been quoted either literally or by content from the sources used. The text document uploaded to TUGRAZonline is identical to the present master's thesis.

Graz, _____ _____

Date Signature

Preface

In the course of this work I was supported and guided by a number of people and institutions to whom I would like to express my gratitude:

First of all, I want to thank the director of the Institute for Materials Science and Welding (IWS) *Univ.Prof. Dipl.-Ing. Dr.techn. Christof Sommitsch*, and my supervisor and deputy director of IWS, *Ass.-Prof. Dr.techn. María Cecilia Poletti*, who gave me the opportunity and encouraged me to accomplish my Master's Thesis at the institute.

I also want to thank the *Faculty of Mechanical Engineering and Economic Sciences* for granting me the *Clever&Smart* scholarship, which made this work and a cooperation with the Institute of Electron Microscopy and Nanoanalysis (FELMI-ZFE) possible.

Furthermore I want to thank the entire team of the institute, the laboratory staff, *Leander Herbitschek*, *Ing. Kurt Kerschbaumer*, *Gernot Stöfan*, and *Thomas Friedl*, who introduced me to the lab's equipment and always advised me during the experimental part of my work. Equal thanks are directed to the junior and senior scientists, especially *Dipl.-Ing. Johannes Tändl*, who willingly shared his experience with EB structuring, and *Dipl.-Ing. Claudia Ramskogler*, who helped me out in one way or another many times.

Special thanks I want to address to *Ao.Univ.Prof. Dipl.-Ing. Dr.techn. Ferdinand Hofer* of FELMI-ZFE, and especially to *Dipl.-Ing. Dr.techn. Julian Wagner*, who guided me through the experiments at FELMI-ZFE.

The greatest thanks however, I want to express to my supervisor *Dipl.-Ing. Dr.techn. Fernando Gustavo Warchomicka*, who actively supported me throughout my experimental work and in writing the present thesis. His immediate feedback was incredibly helpful and he always had a good piece of advice for me.

Finally, I want to thank my familiy, for supporting me throughout my years at TU Graz and my entire life. Without them, my study would not have been possible.

Abstract

In recent times, magnesium and its alloys have been investigated exhaustively for medical application as biodegradable implants. These surgical implants would dissolve gradually, avoiding a second operation to the patient. The improvement of the tissue-implant bonding and the degradation rate control are both strongly dependent on the surface condition of the material. Surface treatments, such as blasting, etching, or plasma coating, among others, are applied satisfactory in different biomaterials. However, the modification of the surface more precisely and geometrically defined is still a field of interest, where the technology of electron beam welding can play an important role.
In this work, surface modification by electron beam (EB) technique is carried out on pure Mg and magnesium alloy AZ91. Structured figures are designed following different criteria in order to develop a specific topography and roughness on the surface.
By deflecting the electron beam repeatedly a short distance over the surface of the material, protrusions are created by moving molten material. The beam deflection is operated by coordinate files, which are compiled by numerical computing (MATLAB). The influences of the surface modification process and its parameters on microstructure and surface of the material is evaluated by topography observations and microstructure analysis.
The height of the resulting structure and the number of simultaneous created pins depend mainly on the beam power and the physical properties of the material. Pins of pure magnesium show a different shape as those pins in the AZ91 alloy due to the lower melt viscosity of pure Mg.
The final shape of the pin structure and the roughness are influenced by the design of the deflection figure, denoted by number of arms, specific geometry and overlapping of swipes, among other considerations.
Smaller grains are observed in the studied materials due to the cooling rate during the pin process. The alloy AZ91 shows in the pin body a homogeneous distribution of the alloys elements with a very fine distribution of intermetallic phases, compared to the base material.
In both materials, cavities within the pin body are observed as a result of the overlapping of the protrusion produced by the beam travel and the cooling rate during the solidification. These cavities can be avoided by a multi-step pin creation in AZ91 alloy, where multiple structures are produced on top of each other. In pure Mg, cavities can be suppressed by beam swipes overlapping the center of the pin.

Kurzfassung

In den letzten Jahren waren Magnesium und seine Legierungen Gegenstand vieler Studien über den Einsatz als abbaubare Biomaterialien. Derartige chirurgische Implantate würden sich mit der Zeit im Körper auflösen, was der Patientin / dem Patienten eine zweite Operation ersparen würde. Die Verbesserung der Körpergewebe-Material-Bindung und die Steuerung der Abbaurate hängen beide sehr stark von der Oberflächenbeschaffenheit des Materials ab. Oberflächenbehandlungen wie Oberflächenbestrahlung, Ätzen oder Plasmabeschichtung werden hierbei erfolgreich an verschiedenen Biomaterialien angewandt. Eine präzise und geometrisch bestimmte Modifikation der Oberfläche ist jedoch nach wie vor ein Interessengebiet, worin die Technologie des Elektronenstrahlschweißens eine wichtige Rolle spielen kann.
In dieser Arbeit wird eine Oberflächenstrukturierungstechnik mittels Elektronenstrahl (*electron beam*, EB) auf reinem Mg und der Magnesium-Aluminium-Legierung AZ91 durchgeführt. Strukturierte Figuren werden nach den folgenden unterschiedlichen Kriterien entworfen, um eine bestimmte Topografie und Rauheit der Oberfläche zu erstellen. Durch wiederholte Ablenkung des Elektronenstrahls über eine kurze Distanz auf der Materialoberfläche werden Oberflächenfiguren durch bewegtes geschmolzenes Material erstellt. Die Strahlablenkung wird durch Koordinatendateien gesteuert, welche mittels numerischer Berechnung (MATLAB) erstellt werden. Die Einflüsse des Strukturierungsprozesses und dessen Parameter auf Materialmikrostruktur und -oberfläche wird durch Topografiebeobachtungen und Mikrostrukturanalyse festgestellt.
Die Höhe der erzeugten Struktur und die Anzahl der gleichzeitig erzeugten Pins hängen hauptsächlich von der Strahlleistung und den physikalischen Eigenschaften des Materials ab. Reinmagnesiumpins zeigen wegen der niedrigeren Viskosität der Reinmagnesium-Schmelze eine andere Form als Pins in AZ91.
Die endgültige Form der Pinstruktur und der Rauheit wird unter anderem durch den Entwurf der Ablenkungsfigur, gekennzeichnet durch Armanzahl, genaue Geometrie und Überlappung der Figurarme bestimmt.
In den untersuchten Materialien werden kleinere Körner beobachtet, welche aus der Abkühlrate während des Strukturierungsprozesses resultieren. Die Legierung AZ91 zeigt eine homogene Verteilung der Legierungselemente mit einer sehr feinen Verteilung von intermetallischen Phasen, im Vergleich zum Basismaterial.
In beiden Materialien werden Hohlräume innerhalb des Pinkörpers beobachtet, verursacht durch die Überlappung einzelner durch den Elektronenstrahl verursachter Vorsprünge und der Abkühlrate bei der Erstarrung. Diese Hohlräume können durch mehrstufige Pinerstellung in AZ91, wo mehrere Strukturen aufeinander produziert werden, vermieden werden. In Reinmagnesium können die Hohlräume durch Überlappung der Figurarme im Pinzentrum unterdrückt werden.

Contents

1 Introduction

The 1940s and early 1950s marked the beginning of professional biomedical technology. The initial objective was to medically treat injuries of the human body by applying internal fixation, such as locking plates or screws. Since then, the technologies have improved significantly, addressing a variety of applications, such as artificial joints, organ parts, and dental implants.
Implants offered a variety of advantages in comparison to conventional, external treatments. On the other hand, medical implants brought along undesired effects or reactions of the human body. Known issues are repulsion of the implant, inflammation, and infection in the vicinity of the implant. Avoiding and dealing with side effects of implants is one big topic in biomedical technology. Furthermore, the application of implants usually requires a removal of the latter, after the healing period. The behavior of cells and bone tissue adherence was and is the subject of many studies.
This work concerns an alternative surface structuring technique by electron beam (EB), in order to enhance the cell adherence and degradation performance of magnesium-based biomaterials. In chapter 2, a literature review of biomaterials technology is presented, to establish a basic understanding of common biomaterials, their biocompatibility and degradation, and the influence of the surface condition on biocompatibility and degradation. Furthermore, the electron beam welding technique (EBW) is presented and the process of creating surface structures with the electron beam is explained.
Chapter 3 describes the performed experiments, starting with the characterization of pure magnesium and the magnesium-aluminum-alloy AZ91. Next, the operation of the electron beam welding equipment and the control of parameters are explained. The design of the beam deflection figures by MATLAB is described, and the different design properties are listed. Finally, the characterization of the produced surface modification is explained.
In chapter 4 the results presented. The influence of the EBW parameters on the produced surface structures is investigated and the pure Mg and AZ91 pin structures are compared to the base material and blind welds. Then, the process influence of parameters on geometry is described, and the limitations are specified. Finally, the achievable surface roughnesses by the structuring process was also investigated.
In chapter 5, a summary of the studied work and an outlook for further investigations is given.

2 State-of-the-art

2.1 Biomaterials

Biomaterials are purposed specifically for the use in medical applications, they are applied as implants, artificial organs, or rehabilitation devices. In general, biomaterials are materials used in applications and devices, where they are in contact with biological systems [1]. Biomaterials which find application as implants are characterized by some additional properties, like biocompatibility or degradability.
The term "biocompatibility", was defined 1987 by Williams as "the ability of a material to perform with an appropriate host response in a specific application" [2]. Biocompatible can mean bio-inert (no or little interaction with the host) or bio-active (desired interaction with the host). The biocompatibility depends on the type of material that is implanted, which is responsible for the interaction between biomaterial and host environment.
The first materials used in biomedical technology were chosen amongst already available materials depending on the clinical application's required properties, while only causing a minimum of host tissue response. Silicon rubber, elastomers, and stainless steels found an early application. The following second generation biomaterials were derived from the gathered experience from the first generation ones, and were designed to trigger a desirable reaction of its host tissue, thus being bio-active. Today's research focuses on the so called third generation biomaterials, specifically engineered to play an active role in the stimulation and aid of the regeneration of functional tissue, and also to truly replace organic tissue [1].

2.1.1 Common Biomaterials

In modern biomedical applications, three types of materials are used: ceramics, polymers, and metals.

Ceramics and Glasses

Ceramics are defined as refractory, polycrystalline line compounds. Ceramics used in biomedical technology are for example Al_2O_3 (alumina) or ZrO_2 (zirconia) [3]. Ceramics are mostly bio-inert, which means, they do not bond directly with living cells. They are used in applications other than implants, like optics (glasses), and instruments, among others. In implant technology specifically, only very few ceramics and glasses are established [1].

Polymers

Polymers represent the largest group of materials used in biomedical applications. Basically all the common plastics like PVC, PP, PU, are used. The wide variety of polymers with various different properties, the easy manufacturing, and the availability of both degradable and sustainable materials make them very versatile. However, in terms of strength and fatigue stress, polymers are in general inferior to metals [1, 3].

Metals

The first metals designed specifically for biomedical applications were vanadium steels, but they showed insufficient corrosion behavior. **Stainless steels** became the commonly used iron based alloys, due to their good corrosion resistance. Steels are also relatively cheap, even the highly alloyed types. However, steels are only suitable as temporary implants, since even stainless steels tend to corrode in hostile environments such as living organisms. **Cobalt-chromium alloys** are resistant to chloride ions and show superior fatigue and ultimate tensile strengths, which makes them suitable for long-term surgical implants, like artificial joints. On the downside, the modulus of elasticity ranges from 220 to 234 GPa being therefore even higher than steel's. This can lead to difficulties in stress transfer into bone tissue, whose modulus of elasticity is about 20 GPa [4]. **Titanium alloys** (Ti) show similar corrosion resistance, fatigue and tensile strengths like CoCr alloys while titanium is a light metal (density about 4.5 $^{g}/_{cm^3}$), and also has an modulus of elasticity of only 115 GPa. Ti6Al4V has become the most widely used Ti based biomaterial for implants. The biocompatibility of titanium is limited, some repulsion effects have occurred with Ti-alloys [3].
A new approach for degradable biomaterials is given by **magnesium and its alloys**. Magnesium is nontoxic and occurs naturally in the human body as a mineral nutrient. The potential of magnesium lies in its degradation potential by the human body. Magnesium based bio-parts could be designed to act as a structural support or fixation device (for instance bone screws) within the human body, and be dissolved after a certain period [5]. Thus, the removal operation of the implanted parts can be omitted. On the other hand, however, the high degradation rate of Mg excludes it from long term implants. Unfortunately, the corrosion process of magnesium is a reaction with chloride containing solutions, causing hydrogen evolution. The hydrogen accumulates in gas bubbles surrounding the implanted material and delays the healing process, sometimes leading to tissue necrosis [6].
The magnesium based alloys currently investigated for biomedical applications are pure Mg, Mg-Al-, and Mg-Ca-alloys. Mg-alloys are used widely in automotive and aerospace applications, and therefore often contain alloying elements which may not be suitable for biomedical applications [7]. The following alloying elements are of potential interest for biomedical applications:
Aluminum (Al) is the most commonly used alloying element of magnesium in industrial applications. Al improves the tensile and yield strengths as well as the hardness. The corrosion resistance however, is below those of Al alloys. In general, Aluminum is

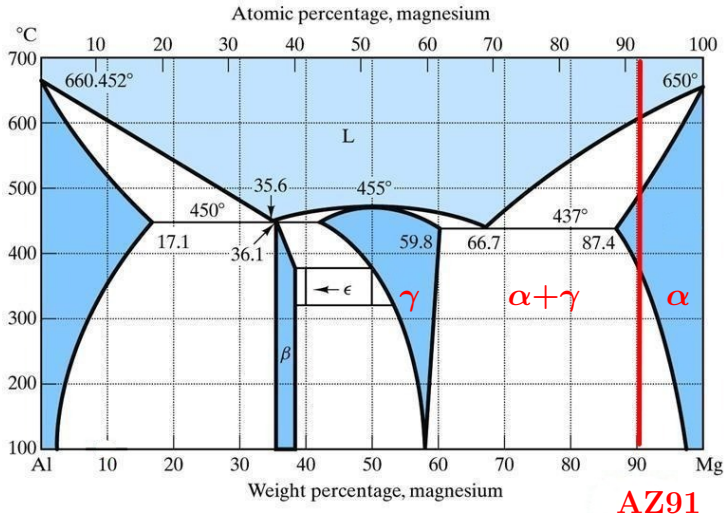

Figure 2.1: Al-Mg phase diagram [13] with highlighted position of AZ91 and indicated areas of α- and γ-phases

considered nontoxic, having a LD_{50}[1] of 6.2 $^{g}/_{kg}$ [8].

Zinc (Zn) has a high solubility in Mg and causes a solid solution- and an aging strengthening effect. The ultimate tensile strength increases with the Zn content, but the corrosion resistance decreases. As the third element alongside Al, Zn is used in the AZ alloys, a type of very widespread Mg alloys, which are applied in automotive, aeronautic and electronic industry. Their main advantage are their good castabilites, and very low density in comparison to other metals [9]. AZ alloys are comparable to aluminum alloys in terms of yield strength and hardness, while its corrosion resistance is below those of aluminum [10]. For observing phase changes, solidus and liquidus, AZ91 can be treated like a binary Mg-Al alloy. The single percent of zinc has little influence on the alloy's properties [10]. The Al-Mg phase diagram in figure 2.1 shows, that within the hcp α-Mg base matrix one main intermetallic phase in AZ91 is expected: bcc γ-$Mg_{17}Al_{12}$. This precipitate is labeled γ in figure 2.1, and contains 43.95 wt.% aluminum, and has with 80 GPa almost twice the modulus of elasticity of the α-Mg phase [11, 12].

Zirconium (Zr) is used mainly as a grain refiner, thus increasing the ductility. It also induces a high damping capacity into the alloy. In respect of degradation, Zr decreases corrosion resistance, and its alloying amount is therefore limited.

Silicon (Si) and Mg form an intermetallic phase which strengthens the alloy in terms of yield and ultimate tensile strengths, more than achievable with any other alloying element. However, Mg-Si-alloys show a radically increased degradation rate.

Calcium (Ca) and **Strontium** (Sr) are of the same periodic table group, which means they show a similar influence on Mg. They refine the microstructure and improve the strength and creep properties. Unfortunately, the precipitates of Ca and Sr are brittle,

[1]The median lethal dose LD_{50} is the point, where 50% of the test subjects exposed to the substance die

which decreases the capacitance of the material for mechanical stress [7].

2.1.2 Degradability of Biomaterials

Degradation is the dissolution of the material by chemical reactions, mostly by electrochemical reactions. In the field of biomaterials, degradability means the dissolution behavior within a living organism. Degradability is desirable, whenever an implant only serves a temporary task, until regenerated tissue fills in. In the past, biodegradable materials were mostly polymers, as polymers are organic compounds themselves and their dissolution residuals are harmless to the human body [1]. Iron and steels are also considered degradable, as iron exists in the human body naturally and can be absorbed. A research from Moravej et al. focused on the degradation of electroformed and casting and thermomechanical treatment (CTT) iron foils, which showed moderate degradation rates [14]. Problems with Fe-based metals are the slow degradation rate observed in animal tests and the ferromagnetism of iron, which limits the compatibility with magnetic resonance imaging [7].
The human body fluid contains, among others, H_2O and chlorine ions, which bear an electrochemical potential. In the degradation process of implants, electrochemical corrosion plays a large role [15]. Some research shows a variation of the degradation rate depending on the actual location of magnesium bone screws, as compiled and assessed by Henderson et al. [5]. Walter et al. [16] investigated the degradation of Mg-alloy AZ91 specimens with different surface roughnesses produced by blasting, and concluded that a rougher surface tends to degrade more locally.

Corrosion

At the degradation process of biomaterials, a few different modes of corrosion can occur. **Pitting corrosion** is a process where localized dissolution of the passivation layer leads to cavities. **Crevice corrosion**, similar to pitting corrosion, appears typically at narrow crevices or under deposits. **Fretting corrosion** is caused by the relative movement of two touching surfaces. The mechanical wear prevents the build up of a passivation layer and thus facilitates the corrosion. Finally, **galvanic corrosion** typically appears at two contacting, dissimilar metals, where the difference in galvanic potential causes the electrochemical process of corrosion [15].
Figure 2.2 shows the electrochemical principle of corrosion in a body fluid environment. The corrosion takes place, wherever a galvanic coupling forms, caused by a potential difference between intermetallic phase and base metal matrix, or grain boundaries (figure 2.2a). Especially the present chloride ions in the body fluid dissolves the protective passivation layers of metals, thus exposing it to proteins, amino acids and lipids, which adsorb into the metal surface and cause the dissolution of the material (figure 2.2b). The breakdown of the passivation layer also causes pitting corrosion (figure 2.2c). It is often observed, that whole grains of Mg disintegrate and drift into the surrounding environment (figure 2.2d) [7].

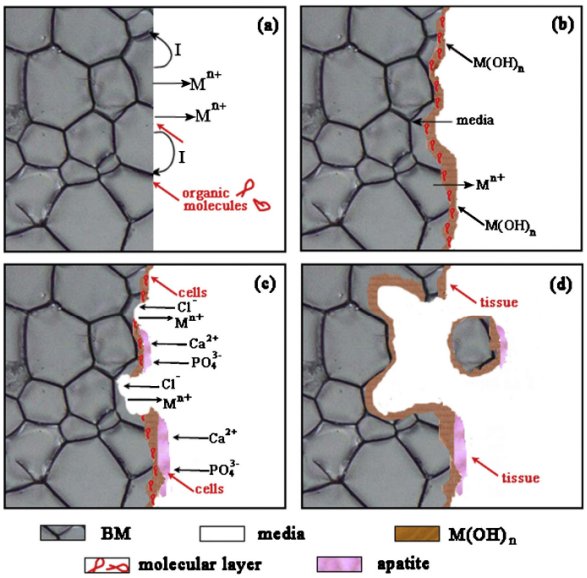

Figure 2.2: Principle of bio-corrosion [7]

2.2 Surface Modification and the Electron Beam Technology

The surface of an implant is in direct contact with the host tissue, and therefore its condition determines the behavior of the implant with respect to its surroundings. The implant-tissue interface has to fulfill certain tasks, such as stress shielding, resistance against wear, the resulting debris from wear, and fatigue failure. The condition of the surface also plays an important role concerning the degradation and corrosion behavior. It has been shown, that a surface modification can improve both the biocompatibility and the degradation behavior [7, 15, 16].

The determining parameters for the degradation are surface roughness, wettability, chemical composition, electrical charge, crystallinity, and mobility [15]. To address the surface roughness in particular, a variety of mechanical, chemical, and physical methods are applied [7]. The surface roughness plays an important role in the biocompatibility and degradability of a material [15].

Machined surfaces are the most basic surface modifications. Milling and grinding, among others, increase microhardness and residual compressive strength which account for the integrity of the material [7].

Blasting is a widely used method on all biomaterials to alter the surface roughness of an implant, where a blast of air and particles abrases the specimen's surface. Depending on the type of abrasive particles used, different surface roughnesses can be achieved. Due to the process, the topography of the surface is always random and irregular, so blasting is not applicable, if a geometrically defined surface is required. Furthermore, depending on the blast particles' material, some negative reactions with residuals from the latter have been reported [15].

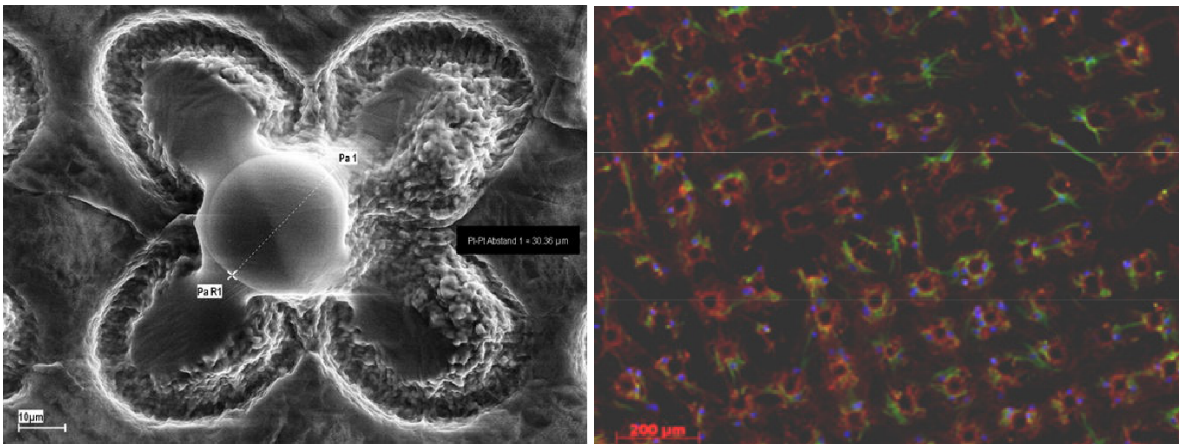

(a) (b)

Figure 2.3: (a) A single micro-figure on TiAl6V4 and (b) stem cell population (fluorescent coloring) in the vicinity of the micro-figures [18]

Acid etching removes the passivation layers from the specimen's surface. Moreover, untreated Ti surfaces tend to form pits at the nano scale. Different procedures have been developed using both agressive and weak acidic solutions to achieve a variety of surface properties. Commonly, etching is used as an additional treatment to, for instance, blasting.
Anodization is typically used to treat titanium based alloys. Anodization is an electrochemical process, where the material is exposed to an ionic solution under an anodic voltage, to promote the formation of TiO_2 layer on the surface. This method is only applicable if a protective layer is formed by the metal.
Plasma spraying is a type of thermal coating, where a hot plasma jet contains particles that fuse and bond at the impact on the surface of the specimen. The bioceramics alumina and zirconia are used for coating to increase the wear resistance of metal implants. Titania, on the other hand, is used to increase the surface roughness. But as most ceramics are bio-inert, the field of application in spraying is limited. Plasma spraying is mostly used in combination with other surface treatments [15].
Surface structures can aid the material-tissue bonding mechanically, similar to composite material joining [17]. Micron level surface structures yield different affinities of surface influence. Reisgen et al. used a modified scanning electron microscope (SEM) to create micro-figures on the surface of a TiAl6V4 plate using the electron beam [18]. It was shown that there is an attraction of cell nuclei to the geometrically defined structures (figure 2.3), rather than a random adherence, common at other treated surfaces.

Surface Treatment of Magnesium and Mg-alloys

Magnesium and its alloys are modified by the means of mechanical, chemical, and physical treatments, like most other biomaterials. A few special treatments for Mg and Mg-alloys can be summarized [7]:

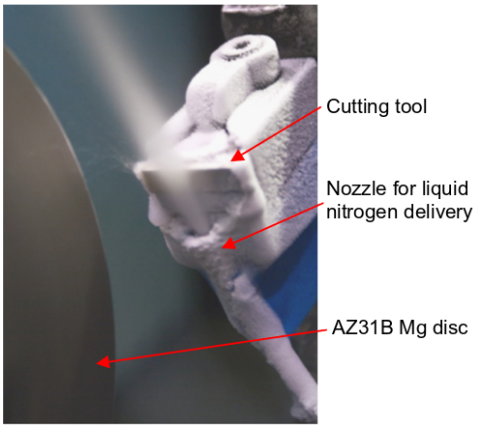

Figure 2.4: Experimental setup for cryogenic machining [19]

The most desirable surfaces for bioapplications among machined surfaces on AZ31B were produced by **cryogenic machining** [19], where the surface temperature is lowered during machining by liquid nitrogen (figure 2.4). Results are grain refinement, roughness reduction, strong basal texture, and higher residual stress. **Chemical treatment** methods on Mg and its alloys are chemical conversion coating, electrochemical treatment, biomimetic deposition, sol-gel treatment, and organic / polymer coating. **Physical methods** include variations of ion implantation (introduction of ions into the surface) and ion or vapor deposition [7].

2.2.1 Electron Beam Welding

Electron beam welding (EBW) is a technique which can address the improvement of biocompatibility by biomedical parts by surface modification. Electron beam welding is a welding technique, where accelerated electrons, focused magnetically, form a high energetic beam to melt material.
Figure 2.5 shows the schematic principle of an EBW machine. The main piece is its beam gun, which produces the electron beam. A tungsten cathode is heated to a certain temperature, and the high voltage between the cathode and the anode forces the emission of electrons towards the anode. The electron beam is accelerated up to about $^2/_3$ of light speed and focused by a series of coils which act as magnetic lenses. The high kinetic energy of the electrons is transferred into the specimen upon impact. Apart from focusing, the coils also allow a deflection of the beam, mainly used for distributing the energy during the weld process.
The high voltage (HV) is a value which is proportional to the electron's achieved velocity. A higher voltage results in a higher velocity. The electrons respond to magnetic fields according to the Lorentz force $\vec{F_L}$:

$$\vec{F_L} = q \cdot (\vec{v} \times \vec{B}) \tag{2.1}$$

where q is the electric charge of the particle (-1 elementary charge (e) in case of an electron), $\vec{v}$ is the particle's velocity, and $\vec{B}$ represents the magnetic field. This means,

Table 2.1: Comparison of maximum power densities of different welding techniques [20]

Heat source	Max. power density $\mathrm{W/cm^2}$
Gas flame	$5 \cdot 10^3$
Electric arc	10^4
Plasma	10^5
Laser beam (continuous)	10^7
Electron beam	10^7

that faster electrons are more influenced by magnetic fields, and thus the electron beam can be focused better by the beam gun's focusing magnetic fields. The beam power P_{beam} is the product of voltage and current (SQ):

$$P_{beam} = HV \cdot SQ \tag{2.2}$$

The advantage of the process is the highly concentrated energy input, which can go as high as 10^7 $\mathrm{W/cm^2}$. Table 2.1 lists the power densities of different heat sources for welding [20]. Due to the high energy density, very deep weldments can be achieved. A single weld beam can produce a weld bead as deep as 40 times its width.
The beam itself has virtually no inertia, which means, it can be deflected instantaneously and very precisely. This allows a very selective heat insertion into the specimen and very precise weldments with very little distortion.

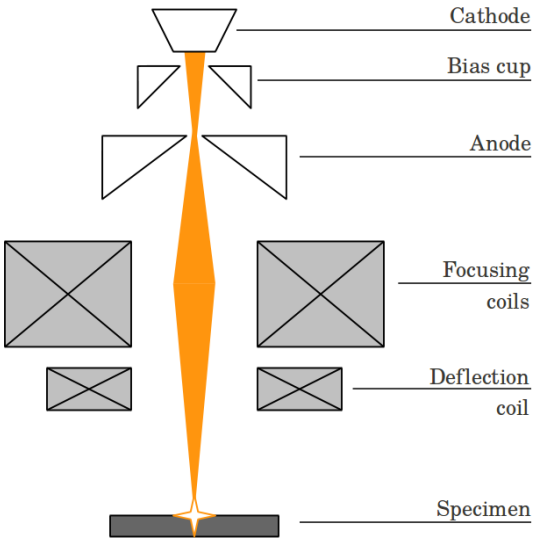

Figure 2.5: Schematic display of an EBW machine

2.2.2 Creating Surface Structures Using an EB

The highly concentrated energy of the electron beam transmitted into the material causes local evaporation and forms a cavity. When the beam travels along the surface, the weld pool and the cavity form a so called "keyhole", that follows the beam. Due to the high pressure within the cavity, the material is pushed backwards, resulting in a protrusion at the beginning and an intrusion at the end of the weldment, as shown in picture 2.6. This effect can be avoided, or amplified, respectively, by control of the process. To avoid a protrusion and an intrusion, a weld start- and end zone with gradually increasing and decreasing welding power, respectively, is carried out.
The surface structuring is based on the effect of creating protrusion patterns by repeating the beam's movement on the same path. In this case, the protrusion and intrusion are raised and lowered, respectively. Moving the beam in several directions away from the center point, a pin-like structure is formed. The result of the latter is shown in figure 2.8, where the electron beam was led in eight directions successively [23]. This technique was first described by Dance and Kellar from TWI, and was referred to as the *surfi-sculpt* process [24]. This process is possible with any focused power beam and was tested both with EB and laser beam [25, 17].
There are several potential fields of application for these structures, one among which is the surface structuring of biomaterials [18]. On the other hand, pin structures can be used in classical and advanced joining techniques, such as COMELD [26, 23], where the pins serve a mechanical interlocking purpose. Considering medical applications, a pin structure could aid the force and stress transfer from the bone tissue into the implant [17], similar to COMELD.

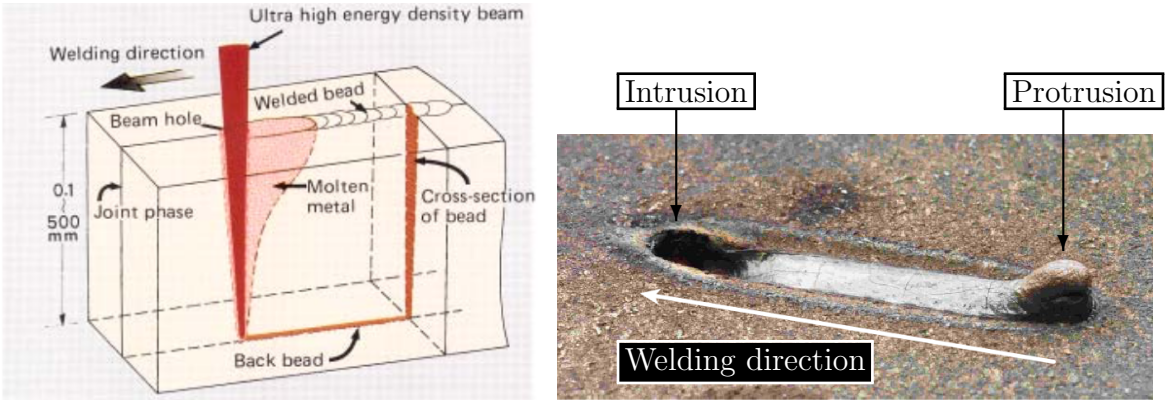

(a) (b)

Figure 2.6: Electron beam welding technique: (a) Keyhole formation [21] and (b) the resulting protrusion-intrusion effect from a single beam swipe [22]

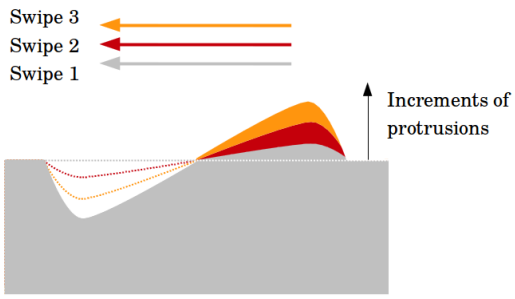

Figure 2.7: Scheme of the effect of repeated beam swipes

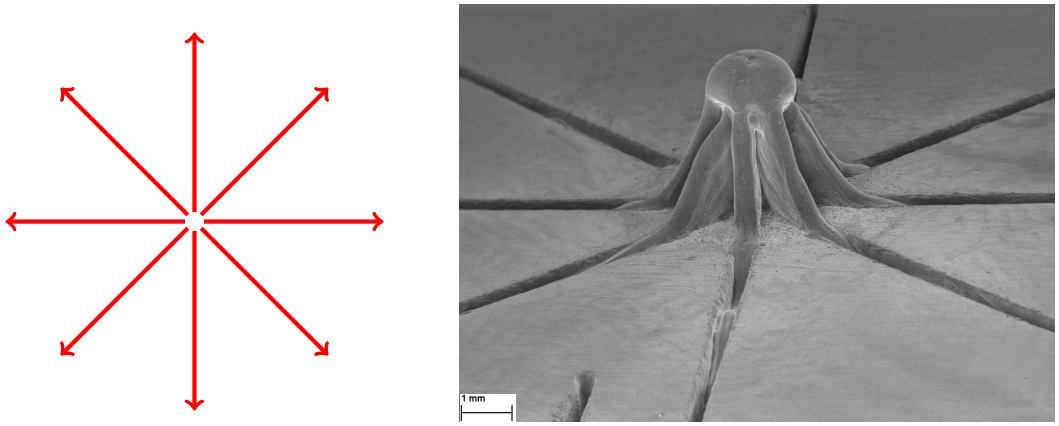

(a) (b)

Figure 2.8: Example of the design of a structure: (a) Star-like beam movement and (b) the resulting surface protrusion [23]

2.3 Motivation

The ongoing research on magnesium and its structuring, lead to the perspective of applying the EB technique on magnesium based biomaterials. The weldability by means of an EBW of magnesium alloys—especially AZ alloys—has already been investigated and has yielded very good results [27, 28]. Some fundamental research about the feasibility of *surfi-sculpt*, both with laser and electron beam in general has been additionally done on Ti alloys, steels, and plastics. The potential of surface structured parts in medical applications has already been suggested elsewhere [17, 25].
The demonstration of surface structuring technique by EB for potential use on Mg based biomaterials, the characterization of the microstructure and surface of the material, and the correlation between weld parameters and structures, are the topics of the present work.

3 Experimental

3.1 Materials

Pure magnesium and AZ91 magnesium alloy were used in the present work.

3.1.1 Pure Magnesium

Pure magnesium itself is rarely used in technical applications due to its low mechanical resistance [10]. However, pure Mg has a potential field of application in biomedical technology. Physical and mechanical properties of pure Mg are shown in table 3.1.

Table 3.1: Physical and mechanical properties of the supplied pure Mg [29]

Property	**Value**
Condition	sand cast
Density	1740 $^{kg}/_{m^3}$
Modulus of elasticity	44 GPa
Specific heat capacity	1025 $^{J}/_{kg\ K}$
Thermal conductivity	159 $^{W}/_{m\ K}$
Melting point	648.3-649.3 °C

In general, pure materials do not possess a melting range (i.e. a different solidus and liquidus point), but a single melting point. This affects the melting and transformation behavior of pure Mg in contrast to any alloyed Mg.

3.1.2 AZ91

AZ91 showed a good biocompatibility at *in vivo* and *in vitro* tests done by Witte et al. [30]. For the EB experiments a plate of AZ91C was provided. The main alloy composition is specified in table 3.2. The letter "C" in AZ91C specifies the ranges of the alloyed materials and impurity limits of trace elements [29, 31]. Physical and mechanical properties of AZ91 are listed in table 3.3.

Table 3.2: Normal composition and impurity limits of AZ91C [29, 31]

Element	**content**
Mg	base (∼90%)
Al	8.1-9.3 wt.%
Zn	0.4-1.0 wt.%
Copper, Cu	$\leq$ 0.1 wt.%
Manganese, Mn	$\geq$ 0.13 wt.%
Nickel, Ni	$\leq$ 0.01 wt.%
Silicon, Si	$\leq$ 0.3 wt.%
Others, total	$\leq$ 0.3 wt.%

Table 3.3: Physical and mechanical properties of AZ91 in sand cast condition [29]

Property	**Value**
Density:	1810 $^{kg}/_{m^3}$
Modulus of elasticity	44.8 GPa
Yield tensile strength:	90 MPa
Ultimate tensile strength:	196 MPa
Specific heat capacity:	1047 $^{J}/_{kg\ K}$
Thermal conductivity:	72.7 $^{W}/_{m\ K}$
Solidus:	470 °C
Liquidus:	595 °C

3.2 Electron Beam Welding (EBW)

Electron beam welding technique was used to modify the specimen's surface and to produce surface structures. The EBW machine *Kammeranlage K14* from *pro-beam* (figure 3.1) utilized in the experiments can produce a beam power up to 45 kW and its modular beam gun can be mounted horizontally or vertically. The vacuum pumps, table motion feed, and the beam deflection itself are controlled by a numerical control (NC) unit. Technical specifications are listed in table 3.4.

Table 3.4: *pro-beam K14* machine technical specifications

max. beam power (P)	45 kW
max. voltage (HV)	150 kV
max. beam current (SQ)	300 mA
chamber volume	1.4 m^3
operation vacuum	$5 \cdot 10^{-4}$ mbar
beam deflection speed	1 $^{\circ}/_{\mu s}$
min. beam focus	0.1 mm
beam current increment	0.1 mA

Figure 3.1: *pro-beam Kammeranlage K14* electron beam welding equipment

In the vacuum chamber, a clamping device was used to fix the specimens during welding, as well as to determine the absolute level for focusing the beam.

3.2.1 Beam Deflection

The fast beam deflection allows the quasi-simultaneous beam creation, where two or more weld beads can be created quasi-simultaneously. This rapid beam deflection function was used to lead the beam in a star-like shape and to achieve surface protrusions, as described in section 2.2.2.
The beam deflection routine interprets coordinate data in the range from 0 to 65,535 increments in both X and Y direction, while the actual dimensions (X- and Y-amplitudes) of the figure are determined separately in a NC program. The coordinate data is read line-by-line from a plain text file, while X and Y coordinate values are separated in-line by a tabulator. The read rate of the coordinate file is also set in the NC program, and combined with the length of the file containing the coordinate points, determines the time required to travel the deflection figure entirely. For example, a deflection file containing 40,000 lines read with a rate of 20,000 Hz (meaning 20,000 lines per second) takes 2 seconds to be completed.
The welding time, on the other hand, is specified separately in the NC program. Taking the previous example—a requiring 2 s for one full cycle—if a second sweep was desired, the weld time would have to be set to 4 s. Figure 3.2 shows a chart, how the machine parameters are calculated from the characterizing values:

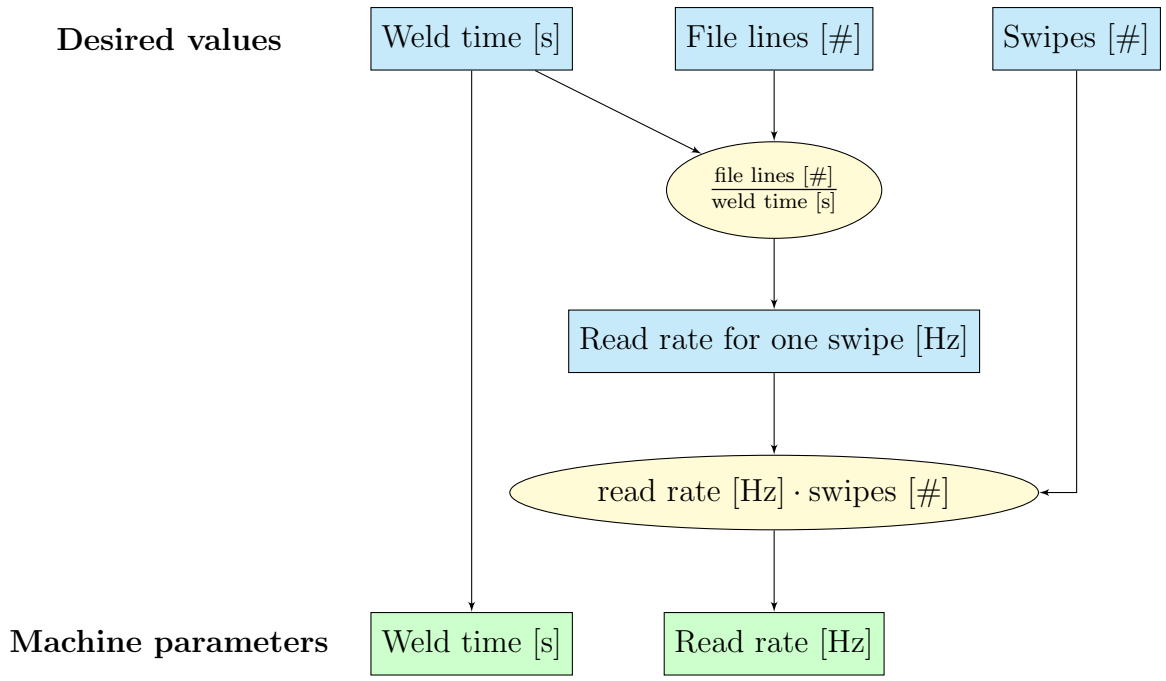

Figure 3.2: Calculation of machine input values from desired structuring parameters

3.2.2 Structuring Parameters

For the structuring process itself, the following parameters were set:

- Voltage (150 kV)
- Beam current (0.1-3 mA)
- Welding time (1-10 s)
- Deflection figure
- Overall structure size (deflection figure X- and Y-amplitudes in mm), with single structure diameters from 1 to 5 mm
- Deflection file read rate (5-40 kHz)

The combination of voltage, beam current, welding time, and the number of swipes were used to describe the surface structures.

3.3 Surface Structure Geometry

The design of a surface structure consisted of three main steps:

- The adjustment of the structuring parameters, denoted by voltage, beam current, file read rate, and welding time.

- The generation of a basic structure geometry.
- The sizing of the structure by setting the X- and Y-amplitudes.

The coordinate files which drove the beam deflection were created by numerical computing. MATLAB was used to program routines for compiling deflection files. The following criteria of design were used for the structuring of the surface:

Arm Number

The arm number is the amount of beam swipes that create a surface structure. Figure 3.3 shows two structures with different numbers of arms. The total travel distance is directly dependent on the number of arms. Therefore, if a structure with more arms is created using the same time as a structure with fewer arms, the beam travel speed will increase. Arm numbers from 6 to 300 were tested.

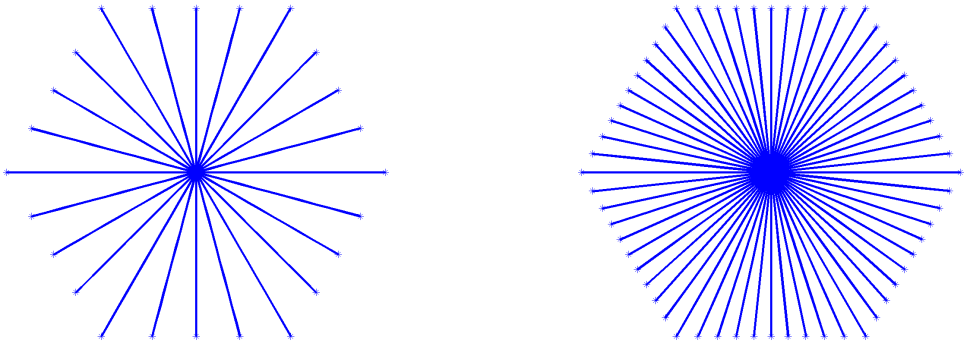

(a) (b)

Figure 3.3: Deflection figures with (a) 24 arms and (b) 60 arms

Arm Overlap

Typical pin structures are created by leading the beam from the center to the perimeter of the geometry, as explained in section 2.2.2. If the structure arm starts before the center of the structure and is drawn over to the opposite side, an overlapping area in the center of the structure is observed, as illustrated in figure 3.4. The overlap was measured in percent of the structure's radius, using overlapping from 0 to 25% in this work.

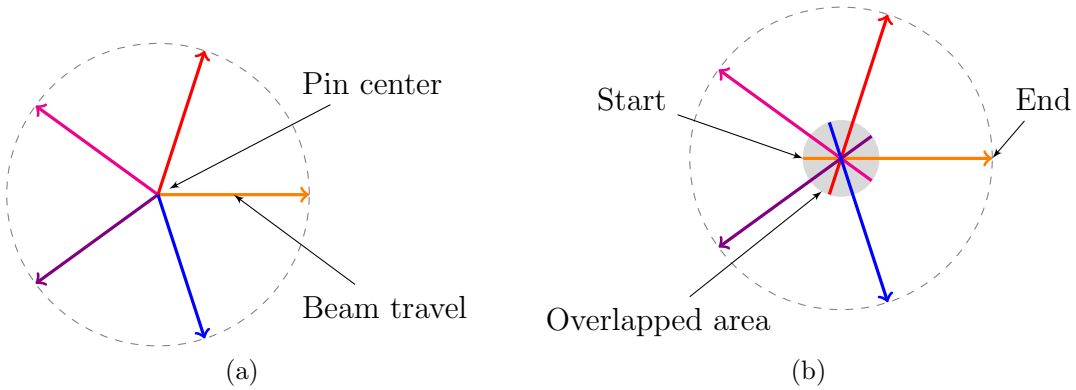

Figure 3.4: Deflection figures with 5 arms: (a) Regular five arm beam travel paths starting at the center, (b) design with 25% overlap

Spiral Arms

The structures of the arms can be straight (figure 3.3) or curved (figure 3.5). Curved arms require longer traveling of the beam, although the total area structure remains the same. Figure 3.5 shows an example of a designed 60° spiral structure, which means, that every arm end point is rotated 60° away from the direction of the arm at the origin. Experimental structures with spiral angles from 30 to 120°—both clockwise and counterclockwise—were produced.

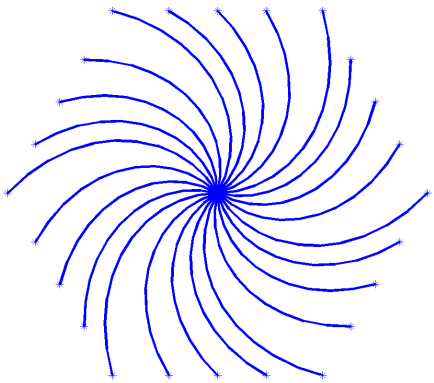

Figure 3.5: Deflection figure with a 60° counterclockwise spiral

Point Spacing

The figure coordinate files are created with an equal amount of coordinate points per arm, which leads to a different spacing between the coordinate points, depending on the arm length. This causes a fluctuation of the beam travel speed, according to the present arm length. An example of a triangular figure shows a wide variation in arm

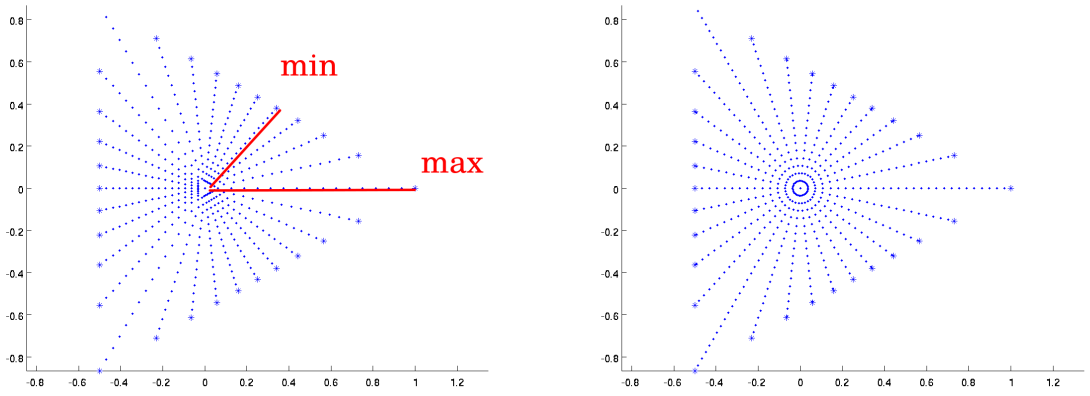

(a) (b)

Figure 3.6: Triangular deflection figures with axes normalized to $(-1, 1)$, (a) same amount of points per arm with minimum and maximum arm lengths remarked and (b) equal point spacing

lengths. The shortest arm is $\cos 60° = 0.5$ times the length of the longest arm (figure 3.6a). To keep a constant beam travel speed, the deflection structure requires an equal point spacing rather than an equal amount of points per arm. Figure 3.6 displays the difference between a constant point spacing and the same point amount for each arm.

Beam Travel Direction

In general, the beam moves from the center to the perimeter (figure 3.7a), creating a surface protrusion. If the direction of the beam is inversed to move inwards, (figure 3.7b), the material displacement effect of the beam results in an intrusion structure. Structures with both outward and inward travel directions were created.

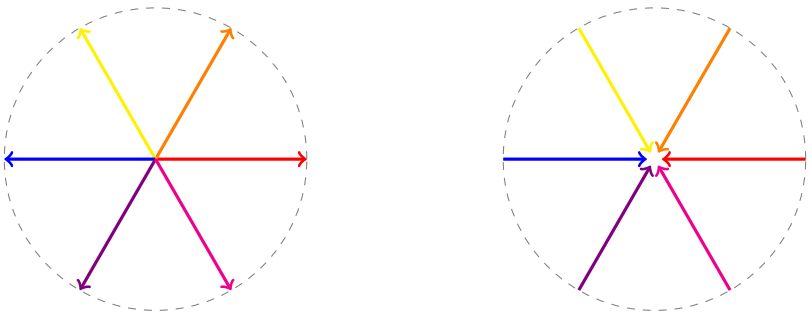

(a) (b)

Figure 3.7: Beam travel direction (a) outwards and (b) inwards

Array Arrangement

To create multiple structures simultaneously, the beam is deflected to travel the first arm of every single structure successively before starting over at the second arm of the first structure, as indicated in figure 3.8.

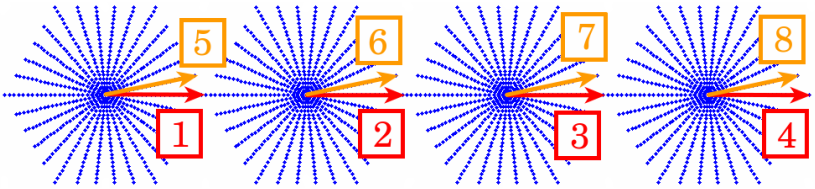

Figure 3.8: Simultaneous creation of four structures (4x1 array), with the swipe sequence from arm 1 to arm 8 denoted

Different geometries can be arranged to cover the surface. In the case of circular structures (figure 3.9a), there is not full structuring of the surface. Triangular- and square-shaped structures can be arranged adjacently to each other. Hexagons can form a honeycomb structure, which show a better inter-connectivity between the figures, as shown by the red line in figure 3.9d. In the present work, arrays of circular, triangular, and hexagonal structures were produced.

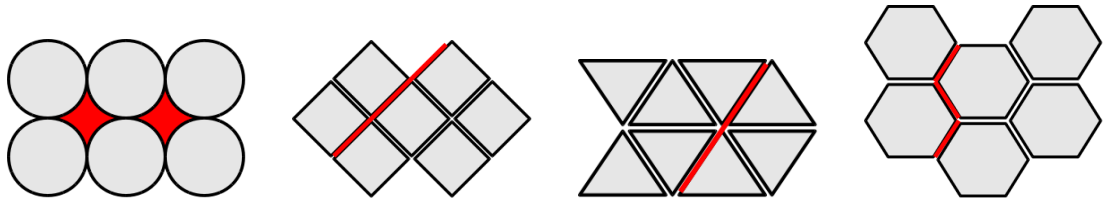

Figure 3.9: Arrays of different structure, (a) highlighting the non-modified surface of circles, (b) possible shear layers of squares and (c) triangles, and (d) a perimeter line of a honeycomb array

Array Combinations

Structures of few arms can cover the surface partially, leaving free space for an additional structure array. Figure 3.10 illustrates the tested combination of a 6-arm hexagon (a so-called "flake" structure) array, filling the remaining space with triangular structures.

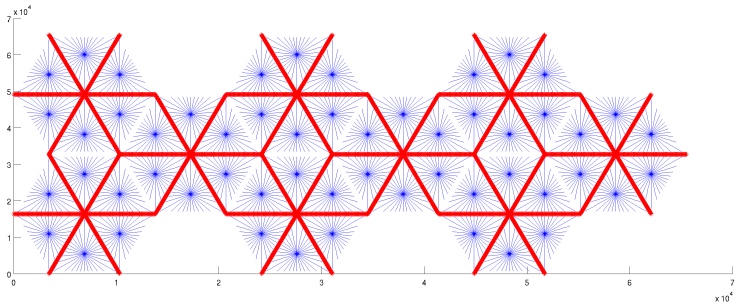

Figure 3.10: Array combination of 9 flakes (red) and 54 triangles (blue)

Swipe Number

As explained in figure 3.2, the number of swipes is determined by the line count of the deflection file and the read frequency. A 40,000 line file read at 40 kHz will cycle in 1 s. The weld time set to 2 s will result in the beam traveling the figure a second time as the machine's read routine starts over at the first line of the deflection file, as illustrated in figure 3.11. Swipe numbers from 1 to 8 were applied in the experiments.

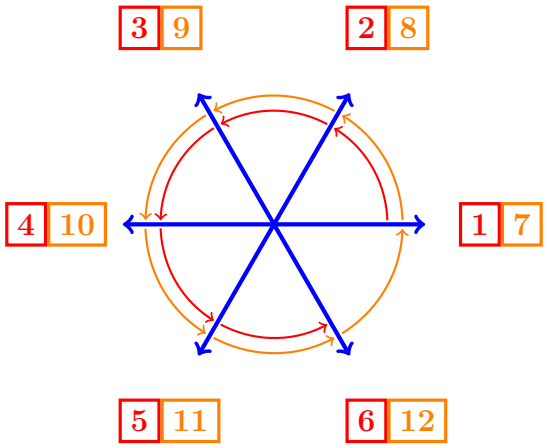

Figure 3.11: Process of two swipes, first swipe (red) and second swipe (orange)

Multi-step Pin Creation

Usually, surface structures are created by one single process with fixed machine parameters. A multi-step pin creation simply means, that the same (or a similar) deflection figure is used to modify an already created structure. The deflection figures and machine parameters can be combined in countless different ways. Therefore, for assessing the effects of multi-step pin creation, the experiments were focused on the following sequences:

- Pre-heating of the surface to allow the melting of the material
- Smoothing the pin's surface after the structuring process
- Creating a three-step pin with different parameters for each step

3.4 MATLAB

In order to create a structured surface with the EBW-machine, the beam has to be led in a certain path, which is carried out by the machine's beam deflection. The input data is a table of two-dimensional coordinate values in a plain text file. This file then is read line by line by the machine's control unit in a selectable frequency.
To create pins, the deflection coordinates themselves are derived from a desired, modeled figure. For this kind of mathematical operations, MATLAB promised to be best suitable. The following steps were considered to create a designed surface as designed in section 3.3:

Creating a Basic Structure

The MATLAB script features the following input parameters to create structures with different attributes:

`corners = 6;`	Type of polygon shape (here: 6 = hexagon)
`arms = 30;`	Number of arms of the structure
`points = 1000;`	Total coordinate points of the structure
`overlap = 0;`	Arm center overlap in % of arm length
`spiral_angle = 90;`	Spiral angle, positive numbers mean clockwise arcs
`equal_spacing = 0;`	Set to 1 for distributing the coordinate points equally

The script executed with these parameters results in a coordinate matrix, as visualized in figure 3.12. The varying space between the arms at the hexagon's corners are a result of the spiral's calculation, where the angle between the arms' origins is always the same. The number of arms and the amount of points are both rounded down to an equal number per polygon segment, or arm, respectively. (for example: Input: 100 arms, hexagonal structure; Output: $100/6 = 16.67 \approx 16$ arms per segment, thus $16 \cdot 6 = 96$ arms)

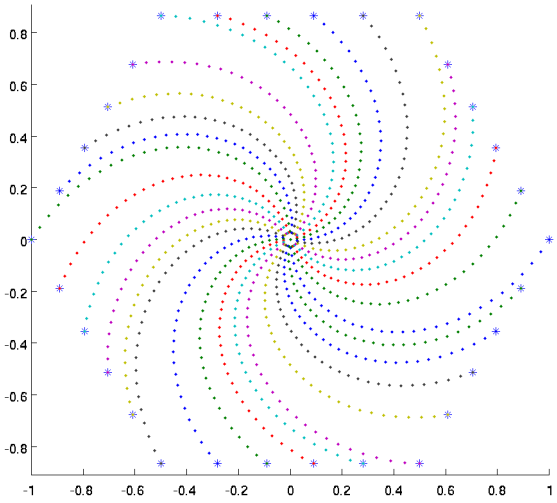

Figure 3.12: MATLAB plot of the created structure with dimensionless axes in the interval $(-1, 1)$: hexagon, 1,000 points, 30 arms, 90° forward spiral

Creating a Structure Array / Writing a Coordinate File

Single structures can be arranged in an array by setting a number of parameters in a second script:

`x_number = 3;`	Array columns
`y_number = 3;`	Array rows
`x_offset = 3;`	Distance in x-direction between structures
`y_offset = sqrt(3)/2;`	Distance in y-direction between rows
`x_displacement = 1.5;`	Shift rows alternately

These options result in the structure array displayed in figure 3.13.

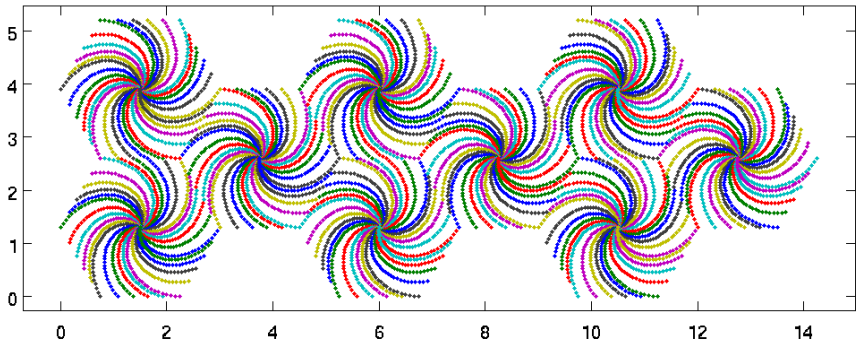

Figure 3.13: MATLAB plot of the created array (stacked 3x3 array of figure 3.12 spiral structure)

Creating a coordinate file readable directly by the EBW machine requires some machine specific parameters:

`filename = 'demonstration.b01';`	Defines an output file name
`polygon_diameter = 3;`	Only required for beam travel calculation
`x_machine_max = 65535;` `y_machine_max = 65535;`	Machine coordinate transformation

The output file *demonstration.b01* contains the calculated and transformed beam deflection coordinates, and can be directly interpreted by the control of the EBW machine. Along with the coordinate file, the script writes an additional plain text file with a *.info* extension. This file contains a summary of all the used parameters, to identify the associated coordinate file.

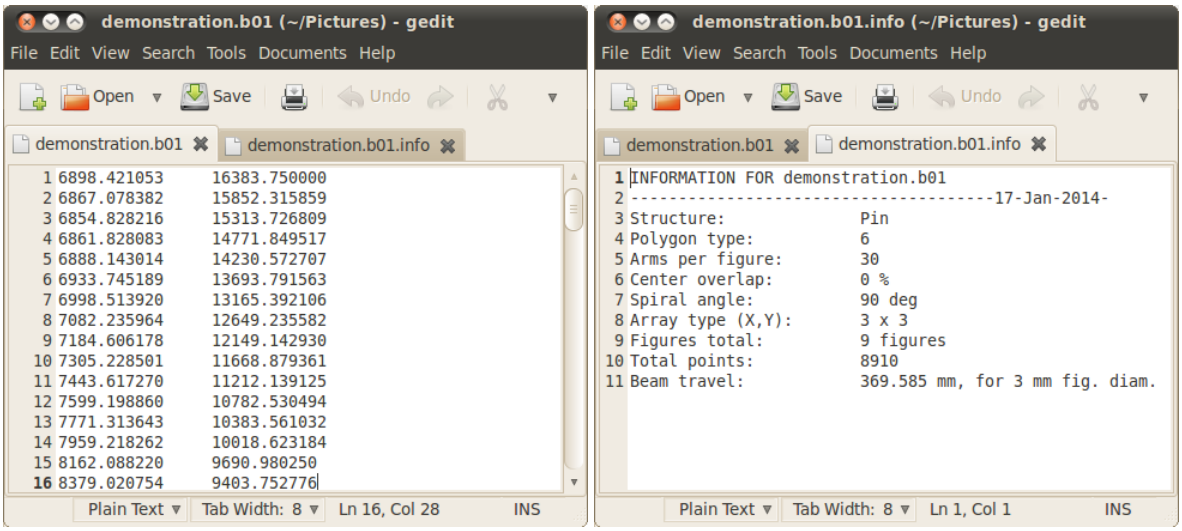

(a) (b)

Figure 3.14: Example of output files written by MATLAB, (a) coordinate file (*.b01*) and (b) summary file (*.info*)

The travel distance of the beam written in the information file is calculated according to the pin diameter value input of the MATLAB-file. The real travel distance depends on the dimensions of the structure and it is not automatically the same as the calculated travel distance.

3.5 Characterization of Surface Modification

3.5.1 Topography

The shape of the created surface structures was documented and evaluated by macroscopic pictures, detailed views by stereo microscopy and selected detailed pictures by a

scanning electron microscope (SEM) to determine inhomogeneities on the surface and to analyze the roughness qualitatively.

3D-profile Recording

An *Alicona InfiniteFocus* microscope was used to quantify the surface roughnesses. This microscope features a special focus variation technique, which allows creating a 3D profile of the observed surface. The device focuses step by step from low level to high level, and calculates the current relative height z (figure 3.15). Every X, Y coordinate point that appears focused, gets assigned the current height. Eventually, a complete three-dimensional topography mapping is created. The appending software *Alicona IFM 2.0* allows a processing of the data for surface profile analysis, to display 3D plots, to create both area and line profiles, and to filter the data to obtain roughness profiles.

(a) (b)

Figure 3.15: (a) *Alicona* principle: Determination of the topography data by focus variation and (b) 2D map of the surface, denoted by contour lines

Surface roughness

For surface roughness characterization, R_a is most commonly used in mechanical engineering. It resembles the arithmetic average of absolute values (equation 3.1) [32]:

$$R_a = \frac{1}{n}\sum_{i=1}^{n}|z_i| \tag{3.1}$$

Figure 3.16 illustrates a schematic roughness profile. This simple profile (black line) is divided into two elementary sine functions—the roughness and the waviness—as displayed in red and blue, respectively.
On real surface profiles, a high-pass filter (for roughness) or a low-pass filter (for waviness) is applied. The key value in both operations is the *cutoff* λ_C, which is the point where a function with that wavelength is damped by 50%. The cutoff therefore distinguishes between roughness and waviness. For comparable results, the cutoff has to be set the same value in different analyses. The value can be chosen arbitrary, in the present work $\lambda_C = 250$ μm yielded the best distinction results.

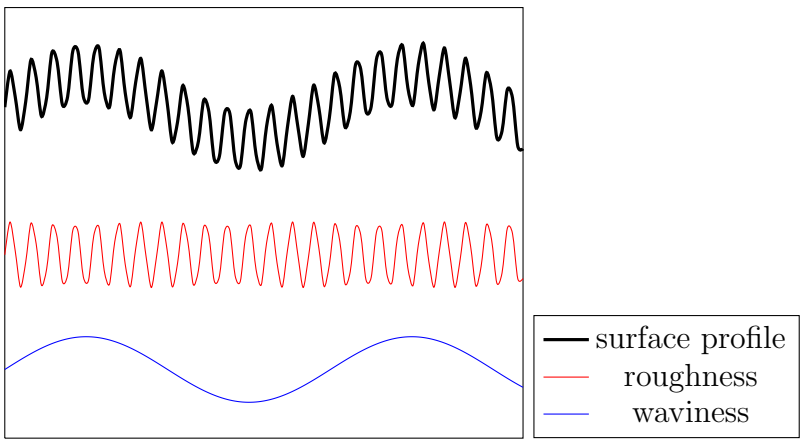

Figure 3.16: Exemplary surface profile and division into roughness and waviness

At the *Alicona* microscope, the maximum vertical resolution depends on the objective lens utilized. A high vertical resolution is favorable, but on the downside implies a longer time to fulfill a recording. For comparison, the same course of a 100 arm structure on pure Mg was recorded with a 5x, a 10x, and a 20x lens. Table 3.5 shows the applied resolutions and required recording times.

Table 3.5: *Alicona* resolution and acquisition parameters

Objective lens	5x	10x	20x
Vertical res. [nm]	392	100	50
Lateral res.[μm]	5	3	1
Acquisition time	10 min	30 min	5 h

Figure 3.17 illustrates the acquisition data of the surface profile by a 5x and a 20x objective lens. Both measurements match qualitatively, observing a slight difference in the depth z due to the resolution and the line scan location. The calculated surface roughnesses R_a were 5.21 and 5.19 μm, by 5x and 20x, respectively. The data obtained with the 5x lens was enough resolution for roughness ranges down to 0.4 μm, due to the vertical resolution. To be able to analyze roughnesses below 0.4 μm, a 10x objective lens was chosen.

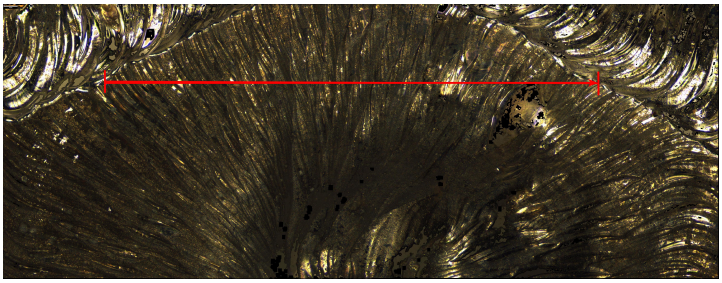

(a)

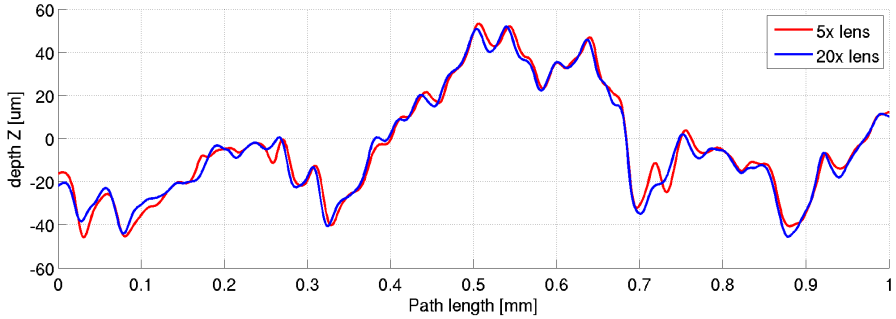

(b)

Figure 3.17: (a) Top view of acquired surface with profile path and (b) surface profiles recorded with a 20x objective lens (blue) compared to a 5x lens (red)

3.5.2 Metallography

Analysis of the microstructural changes, grain sizes, and internal defects was carried out by light optical microscopy (LOM). Energy-dispersive X-ray spectroscopy (EDX) helped to identify the element distribution in the base material and the welded zone.

Sample preparation

The samples were embedded in cold curing plastic frames and ground on abrasive papers of various grit sizes. Subsequently, the samples were polished with a *Struers MD Mol* cloth and 1 μm diamond suspension, followed by a short period on a soft *Stuers MD Chem* cloth with a 1:1 blend of OP-S and ethanol, as listed in table 3.6.
In magnesium preparation, a difficulty to overcome is its tendency to oxidize in contact with water, which produces little black spots on the surface. Therefore, for the 1 μm the water-free lubricant *Struers DiaDuo Lubricant Yellow* was used. For some samples, the OP-S-ethanol was substituted by the water-free *Silica Suspension*.
After the last step of #4000, and between each polishing step, the samples were cleaned in an ultrasonic bath for 2-3 minutes. The *MD Chem* cloth was rinsed with pure ethanol for the last 20 seconds of polishing to remove the OP-S from the cloth and the samples' surfaces. To visualize grain areas, the samples were immersed 5-6 seconds in a blend of picric and acetic acid, with the composition listed in table 3.7.
Pure magnesium preparations should be taken carefully, since on account of its softness

Table 3.6: Sample preparation steps

Grit size, lubrication	**time**	**force per sample**	
320-800, water	various	10 N	grinding
1200, water	3 min	10 N	
2000, water	2x 3 min	10 N	
4000, water	3-4x 3 min	10 N	
1 μm, water-free suspension	2-3x 3 min	10 N	polishing
OP-S or *Silica Suspension*	3 min	10 N	

Table 3.7: Metallographic etching composition [33]

5 ml H_2O
70 ml ethanole
5 ml acetic acid
2.1 g picric acid

and crystalline structure, the slip planes are able to glide along twin layers at room temperature.
For AZ91 preparation, the recipe for grinding and polishing stated in table 3.6 was applied, only pure OP-S was used in the last step. Compared to pure Mg, AZ91 is less susceptible to scratches, and showed intermetallic phases without further treatment.

4 Results and Interpretation of Results

4.1 Base Material

4.1.1 Pure Magnesium

The etched microsection of pure Mg (figure 4.1) revealed magnesium grains up to 3 mm in diameter in the as-received condition. Twinning is also observed, which occurred during the sample preparation by grinding and polishing, due to the applied force.

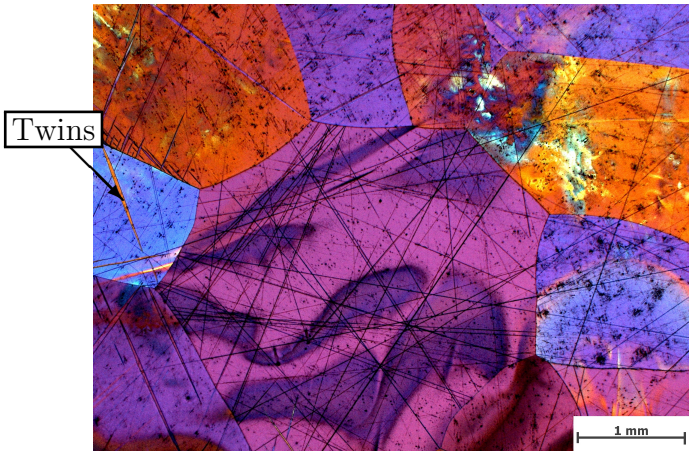

Figure 4.1: LOM image of pure Mg in as-cast condition

4.1.2 AZ91

Figure 4.2 shows the phases in AZ91 alloy. An α-Mg matrix containing γ-$Mg_{17}Al_{12}$ phases of two different shapes are observed (figure 4.2) [9, 11]: A massive γ-phase, which forms directly from the hcp parent phase during solidification, where isolated γ-phases nucleate and grow. The second γ-phase is formed at lower cooling rates and due to eutectic (α+γ) transformation. This lamellar compound of γ- and Al-drained α-Mg phases are formed at grain boundaries and growth into the parent phase. The latter precipitate is less desirable, as it often destabilizes the microstructure due to the easily activated diffusion, which causes a solute redistribution [34, 12]. The etched microstructure in figure 4.3 shows the dendritic structure of AZ91, with grain sizes of 500 μm on average.

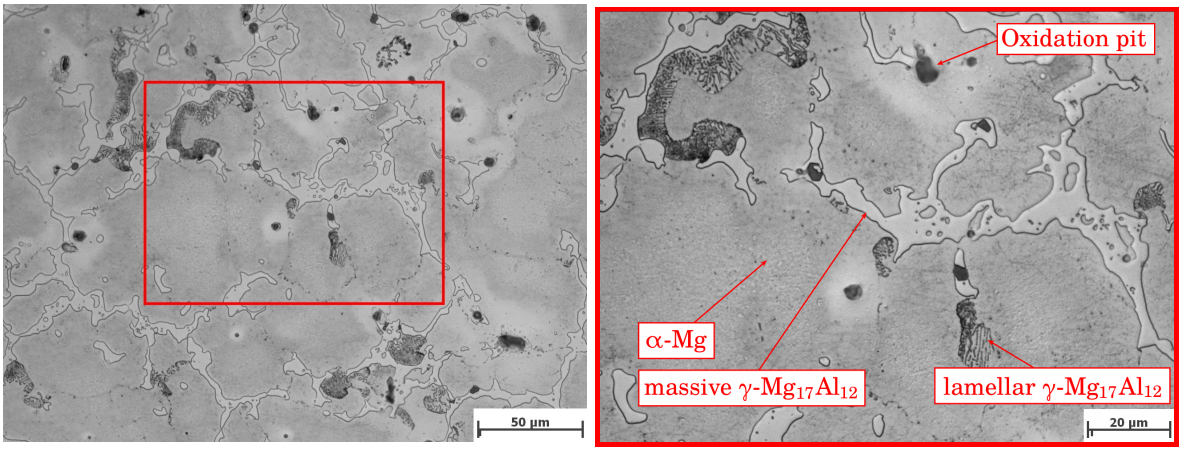

(a) (b)

Figure 4.2: AZ91 in as-received condition, (a) general view and (b) detail of phases

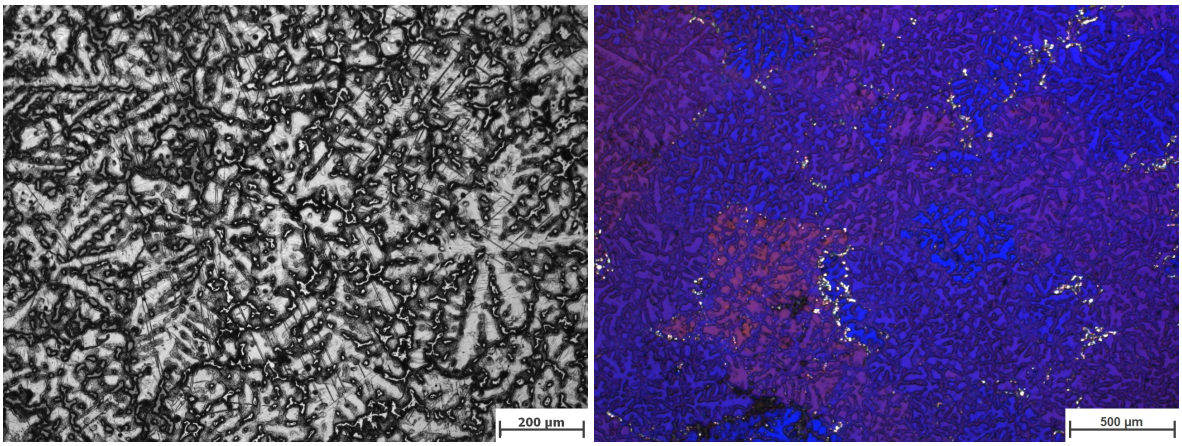

(a) (b)

Figure 4.3: LOM images of AZ91 material etched. (a) dendritic structure and (b) grains visible under polarized light

EDX mapping (figure 4.4) showed the presence of Al in the areas of massive γ-precipitates, in agreement to the literature [34, 11]. Zn is distributed homogeneously throughout the material.

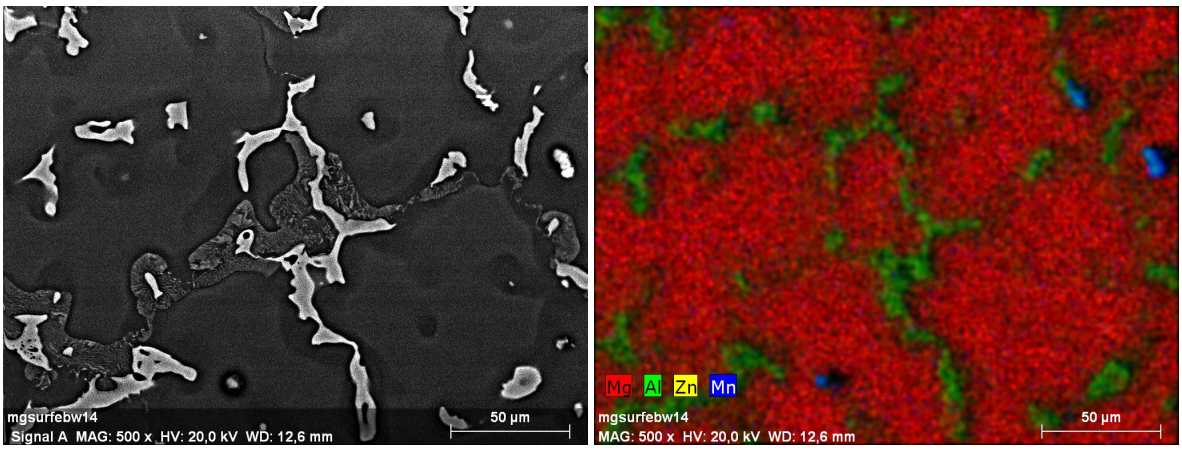

(a) (b)

Figure 4.4: AZ91: (a) SEM image and (b) EDX mapping of element distribution: Mg (red), Al (green), Zn (yellow), and Mn (blue)

4.2 Blind Welds

Microstructure of the pin structure of pure Mg and AZ91 was produced by a series of blind welds. For the blind welds, the beam deflection figure was a circle with a diameter of 0.5 mm, cycled with 300 Hz. The weld length was 30 mm. Figures 4.5a and 4.5b show the blind weld beads on pure Mg and AZ91, respectively.

4.2.1 Pure Magnesium

Figure 4.6 shows a microsection of the blind weld number 4 (figure 4.5a, 6 mA, 10 s) on pure magnesium. The weld beads appear only as small lines through the material, with no HAZ present. The grains of the base material were cut through by the beam, where apparently most of the melt was drained off at the bottom due to the low viscosity of the pure Mg melt [35]. This explains the diminished weld bead of only 0.1 mm width. In the remaining weld bead, grains with a diameter from 10 to 100 μm re-solidified.
Figure 4.7 shows a solidified droplet, spat out onto the surface during the weld process. At the interface between droplet and plate a lack of fusion is observed. The droplet consists of smaller grains due to the high solidification rate.

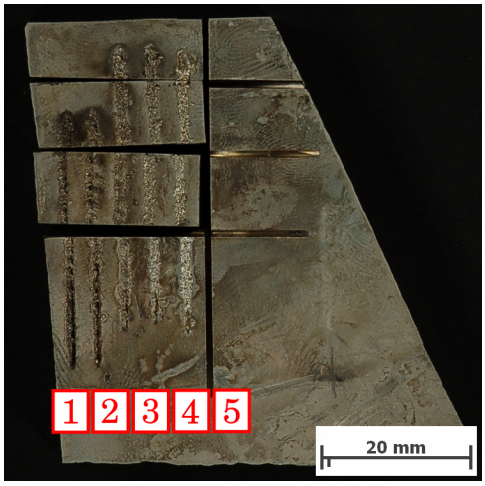

weld no.	current mA	travel $^{mm}/_{s}$	quality
1	6	3	bad
2	6	5	bad
3	6	10	good
4	6	20	good
5	10	20	fair

(a)

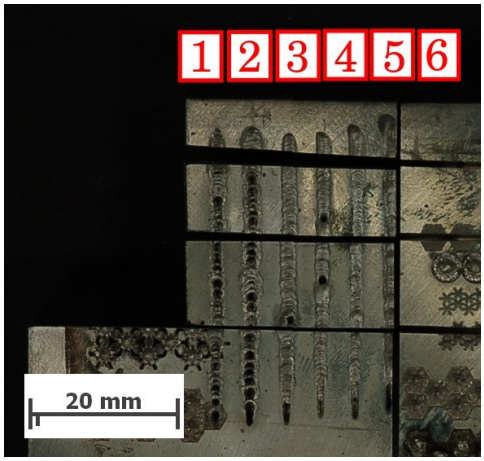

weld no.	current mA	travel $^{mm}/_{s}$	quality
1	6	3	bad
2	10	10	bad
3	6	10	good
4	6	20	good
5	10	20	good
6	15	30	fair

(b)

Figure 4.5: Blind welds, cut work pieces with weld beads and corresponding weld parameters, (a) pure Mg and (b) AZ91

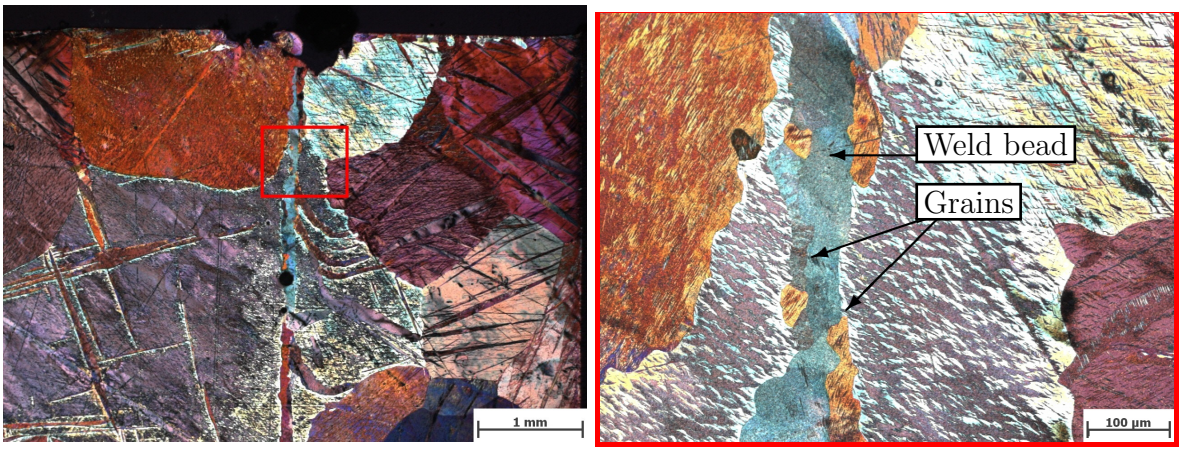

(a) (b)

Figure 4.6: Pure Mg blind weld microsection (a) overview and (b) weld bead

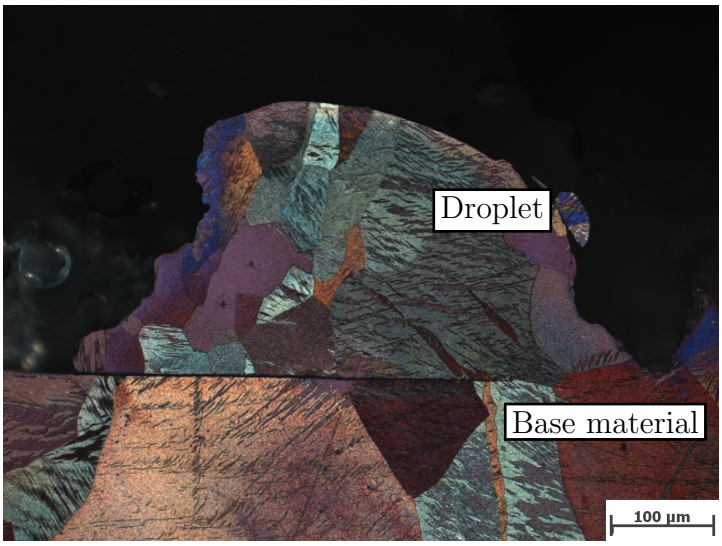

Figure 4.7: Pure Mg solidified droplet of surface from blind weld process

4.2.2 AZ91

The blind weld beads on AZ91 appear in a slightly tapered cross section, with a width of about 1 mm (see figure 4.9). The weld bead (figure 4.9b) bears a fine microstructure, due to a fast cooling after the welding process.
In the HAZ (figures 4.9c and 4.9d), some intermetallic γ-phase melted during the weld process, while the α-matrix remained solid (figure 2.1), and re-solidified in an eutectitc (α+γ)-phase [34] (figure 4.8). The HAZ measured 500 μm in width, on both sides of the weld bead.

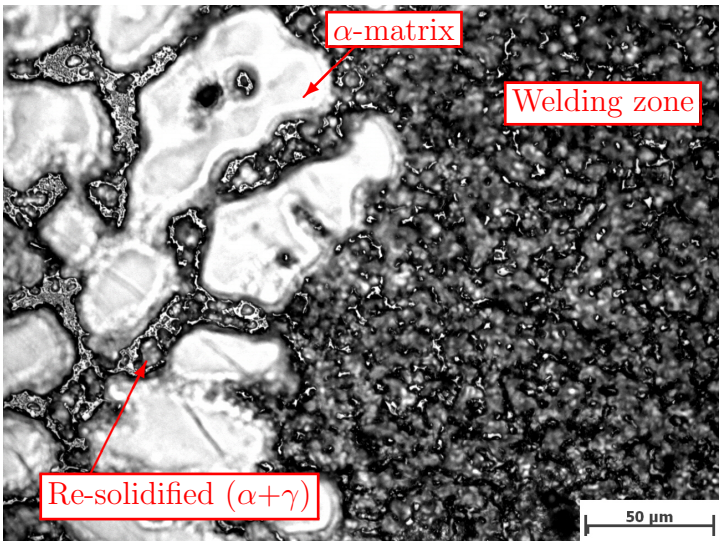

Figure 4.8: AZ91 transition zone from welded area to HAZ with re-solidified phases

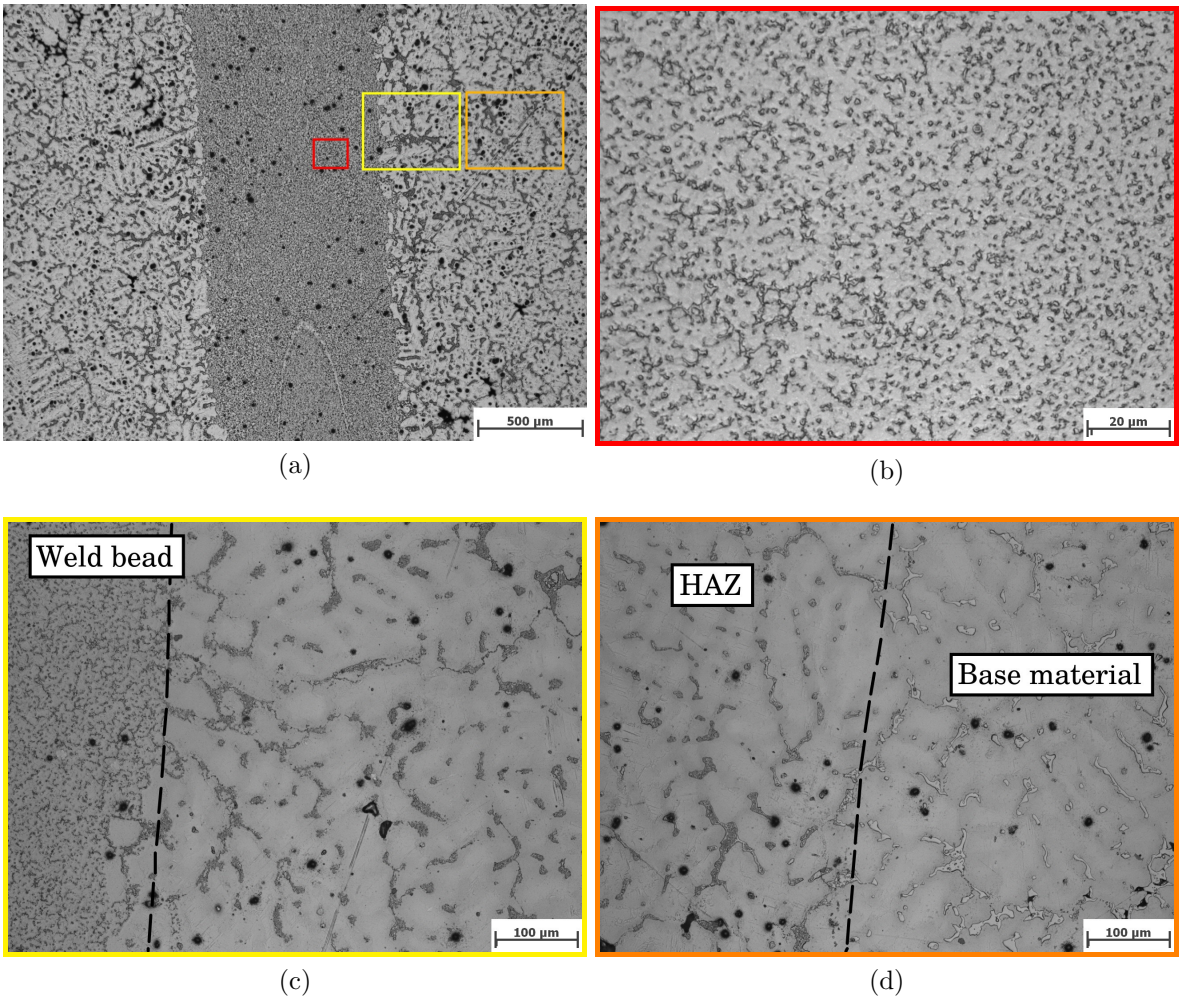

(a) (b) (c) (d)

Figure 4.9: AZ91 blind weld number 4, (a) microsectional overview, (b) detailed weld bead, transition from (c) bead over (c)-(d) HAZ to (d) base material

4.3 Structured Surface

Beam Power

With respect to the welding process, the voltage shows no specific influence or trend in the quality of the weld process [36]. For this reason, the maximum voltage of the machine of 150 kV was used throughout the experiments. With a fixed voltage, the input energy can be modified only by the beam current. The beam current and the consequent energy input had the biggest influence on the pin height. The pin structure design and main parameters are listed in table 4.1 and 4.2.
The *energy input per unit length* is used for measuring the energy distribution in welding processes. It is the quotient of the welding power and the welding speed. In this work that principle results in a direct relation of arm number and energy input per length. Since the arm number did only little effect on pin heights, linking the energy to the

structure array's covered *area*, rather than to the beam's traveled distance, showed a better resemblance of the energy input.
The energy input per unit area (EA) is defined as:

$$EA = \frac{\text{Beam power [W]} \cdot \text{Weld time [s]}}{\text{Covered area [mm}^2\text{]}} = \left[\frac{\text{J}}{\text{mm}^2}\right] \tag{4.1}$$

4.3.1 Topography of Pins

Table 4.1: Weld parameters of beam current experiment

figure type	100 arm pin hexagon
array type	4x1, 16x3.46 mm
current	variable
swipes	1
time	2 s

Table 4.2: Beam current, input energy per unit area, and resulting pin heights

current	**energy**	**avg. pin height**	
		pure Mg	*AZ91*
mA	$^{J}/_{mm^2}$	mm	mm
0.6	3.58	0.00	0.05
0.7	4.18	0.00	0.15
0.8	4.77	0.00	0.18
0.9	5.37	0.00	0.40
1.0	5.97	0.00	0.59
1.1	6.57	0.10	0.73
1.2	7.16	0.20	1.08
1.3	7.76	0.50	1.28
1.4	8.36	0.85	1.41
1.5	8.95	1.35	1.60
1.6	9.55	1.55	1.73
1.7	10.15	1.80	1.71
1.8	10.74	2.20	1.81
1.9	11.34	2.50	1.91

Tables 4.1 and 4.2, and figure 4.10 show the pin height as function of the beam current and energy input, on AZ91 and pure Mg, respectively. The relations of figure 4.10 apply to 4 mm pin diameter, created with a single swipe. For structuring with a different configuration, an according series of experiments is advised. For pure Mg below 1 mA beam current (below 6 $^{J}/_{mm^2}$) the energy was insufficient to erect a pin, only a superficial structuring was observed. The increase of the pin height with increasing current is higher

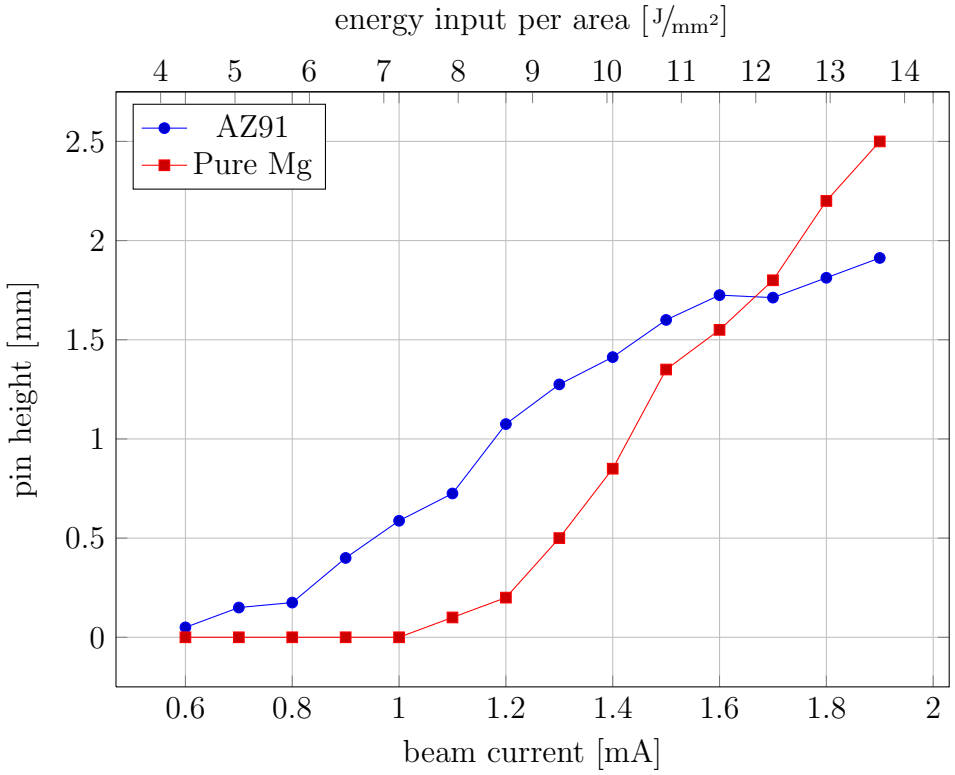

Figure 4.10: Pin height vs. beam current / energy input for pure Mg (red) and Mg-alloy AZ91 (blue).

compared to AZ91. The upper limit for the pins of both materials is about 2 mA, as additional input energy causes a meltdown of the head of the pin, limiting the height to 2 mm (AZ91) and 2.5 mm (pure Mg).
The difference in increasing pin heights for AZ91 and pure Mg can be observed in detail in figures 4.11 and 4.12, which show SEM images of the surface structuring, for beam currents from 1.5 to 1.9 mA for pure Mg (figure 4.12) and 1.1 to 1.5 mA for AZ91 (figure 4.11). AZ91 tends to form a pyramid-like structure, while pure Mg forms thinner pins of the same weld parameters. The reason for the different pin shapes is due to their physical properties. The different response to the structuring process is caused by the remarkably lower viscosity of the pure Mg melt and surface tension than Mg-Al alloys. At same welding processes, AZ91 shows a way smoother and more regular top surface than pure Mg [35].

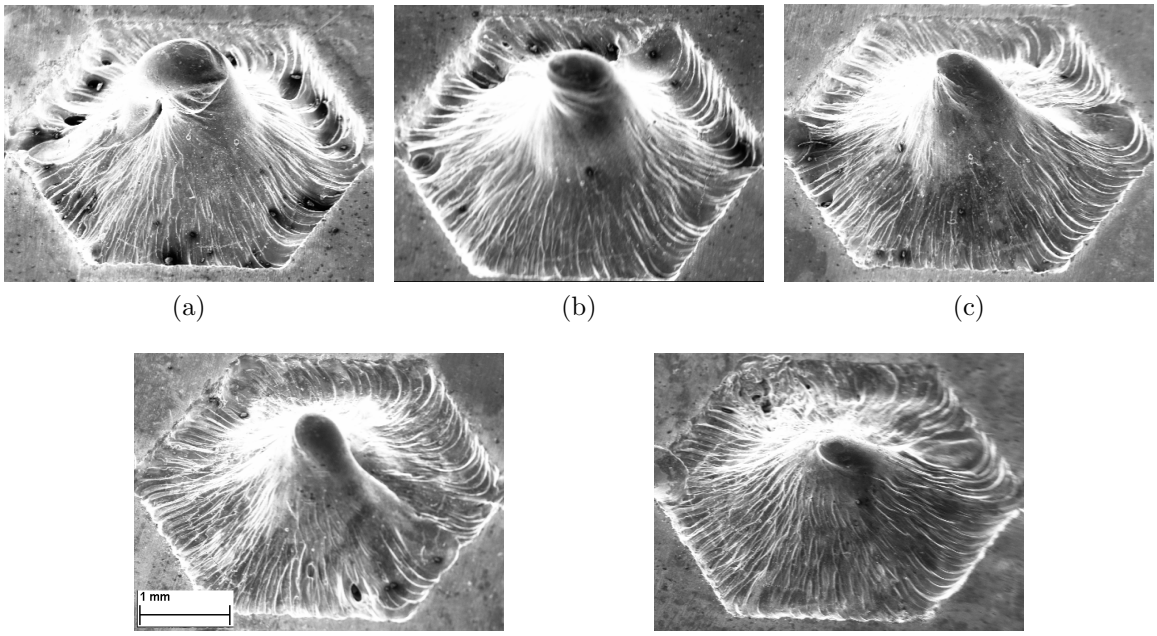

(a) (b) (c)

(d) (e)

Figure 4.11: SEM pictures of AZ91 pin structures with (a) 1.5, (b) 1.4, (c) 1.3, (d) 1.2, and (e) 1.1 mA beam current

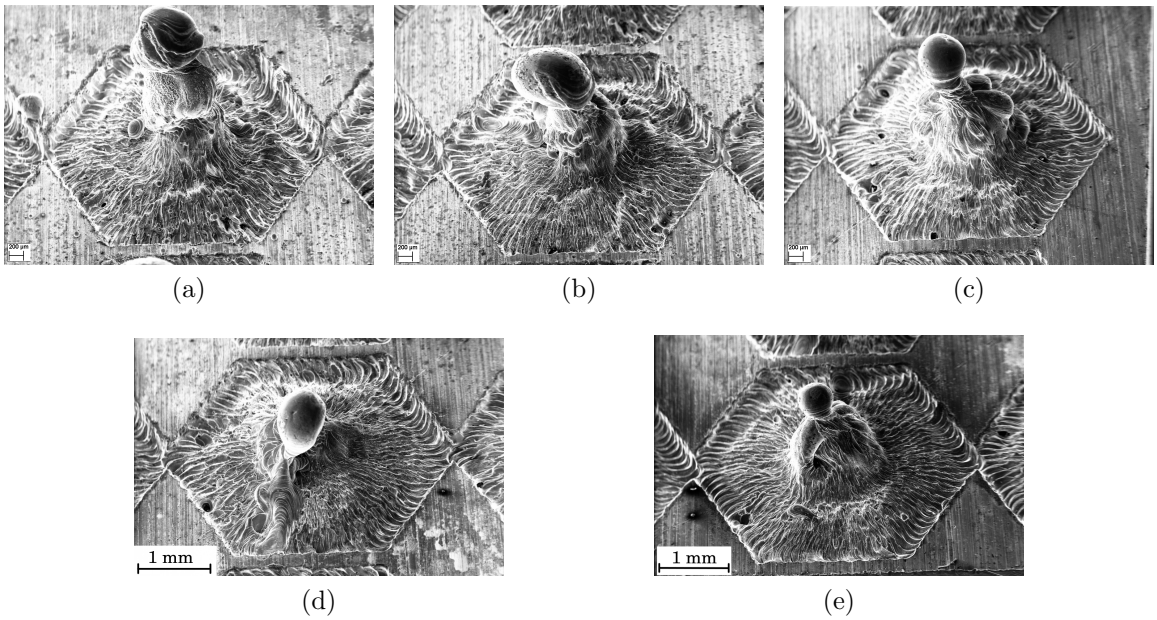

(a) (b) (c)

(d) (e)

Figure 4.12: SEM pictures of pure Mg pin structures with (a) 1.9, (b) 1.8, (c) 1.7, (d) 1.6, and (e) 1.5 mA beam current

4.3.2 Limitations of Figure Size and Energy Input

The most important limit for EB surface structuring is the achievable beam focus. According to the specifications, the machine can focus to a minimum diameter of 0.1 mm. However, this requires a perfect setup of the machine and a perfect focus on the surface of the specimen. In practice, the beam diameter obtained in this work was probably 0.2-0.3 mm, although it was not measured.
To melt the material, a certain amount of heat is required. This means, that there is a lower limit of energy necessary for the pin creation process. The present experiments had shown, that the smallest width that a single weld bead can get is about 0.5 mm, which means, that the beam diameter must be below that value. Figure 4.13 illustrates a weld pool with a beam diameter of 0.3 mm. Figure 4.14 shows the smallest achievable structure with AZ91. Observable at this flake structures with 1 mm diameter are the six weld beads with each structure's arm of about 0.5 mm width. In this case, no surface roughness was observed.
A result of a further reduction of the beam current shows figure 4.15. In this array, the surface has been barely melted, no topography was observed. Compared to a 0.8 mA structure (fig. 4.14) with 18 $^{J}/_{mm^2}$, the energy input was only 9 $^{J}/_{mm^2}$. Hence, the minimum energy input for acquiring a pin structure on AZ91 with a 3x3 flake array was around 10 $^{J}/_{mm^2}$.
On pure Mg, 100 arm star geometries were tested, varying arrays and structure sizes. The graph in figure 4.10 suggested an energy input limit of 8.5 $^{J}/_{mm^2}$ with 4x1 arrays of 4 mm pin diameter. At the experiments carried out with 3x3 arrays of 3 mm pin diameter, as displayed in figure 4.16, no pins were observed at 9.12 $^{J}/_{mm^2}$. At 11.40 $^{J}/_{mm^2}$, a pin creation had taken place. Thus, a smaller structured surface is obtained with a higher energy input per area.

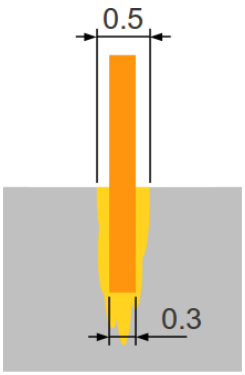

Figure 4.13: EB diameter and the resulting weld pool width

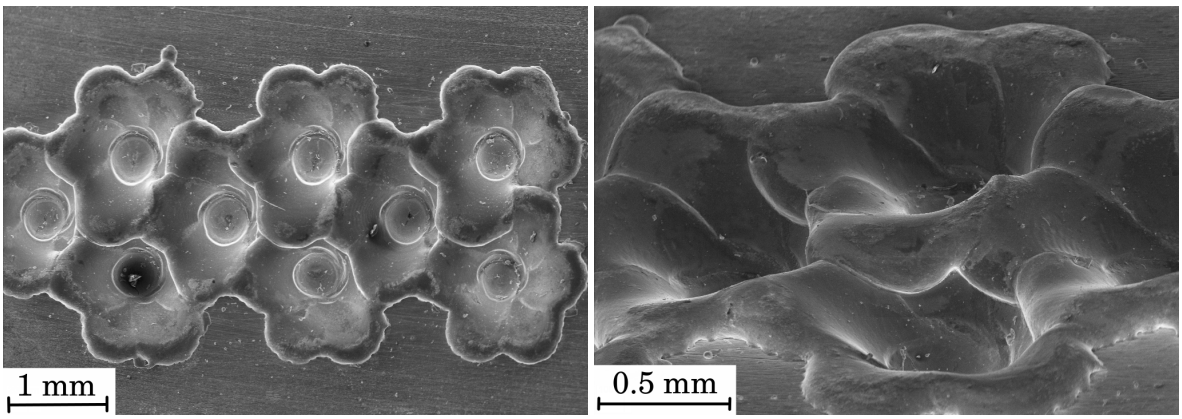

(a) (b)

Figure 4.14: Flake micro-figures on AZ91 (6 arms, 3x3 array, 6x2.6 mm, 0.8 mA, 4 swipes, 4 seconds), (a) top view and (b) topography

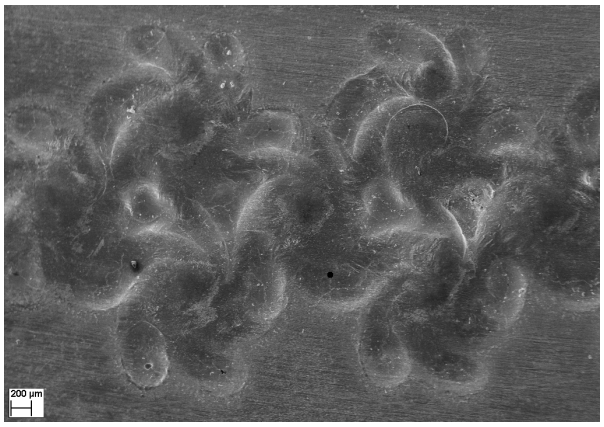

Figure 4.15: Lower limit of micro-figures on AZ91 (3x3 90° spiral flakes, 8x3.46 mm, 0.7 mA, 4 swipes, 4s)

For different materials, the required energy input is a function of the following factors:

- The dimensions of the specimen, influencing the heat dissipation
- Heat conductivity
- Heat capacity

Therefore, it is only possible to predict the structuring behavior with similar geometry and welding parameters.

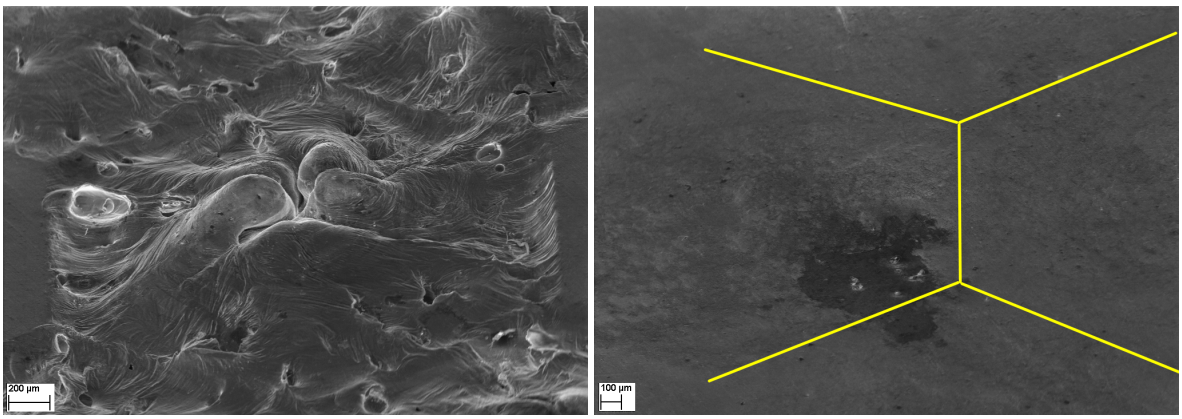

(a) (b)

Figure 4.16: Lowest limit of parameters to get a structure on pure Mg (300 arm hexagons, 3x3 array, 14.25x5.19 mm, 1 swipe, 2 s), (a) 2 mA (11.40 $^{J}/_{mm^2}$) and (b) 1.6 mA (9.12 $^{J}/_{mm^2}$), with the perimeters of the hexagons highlighted

4.3.3 Heat Dissipation

During structuring, the heat must be delivered locally and concentrated, forming a small weld pool. This requires that the base material remains close to room temperature. The structuring is not reproducible when the temperature in the base material increases. An example shows figure 4.17, where several sets of pins were produced successively. At the leftmost set, the pins were not formed properly. This effect was related to the heat transfer. The piece was heated up by previous structuring and was unable to dissipate the heat. Solutions to keep the parts colder are: To allow the parts cool between successive structuring, or to use an active cooling device. In the present experiments, where only small arrays were created, the heat dissipation of bigger base parts sufficed for cooling.

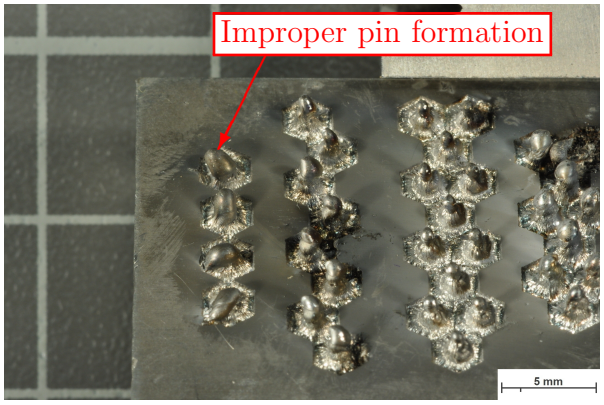

Figure 4.17: Sets of pin arrays, with improper pin creation at higher temperatures of the specimen

4.3.4 Microstructure of Pins

The microstructure within the pins showed a similar refined microstructure as the blind weld bead (figure 4.5). Different areas of molten material could be identified, due to a change in the microstructure pattern, visible by LOM. These different zones resulted from the different origins of the material. The intrusion depth around the pin, denoted in figures 4.19a and 4.19e, is a function of the pin height, the material was shifted to the center and formed the pin.
A HAZ developed at the transition from the pin into the base material, visible by a lamellar precipitate concentration, as observed in figure 4.20. Surface cracks occurred in the outskirt area of the pin, visible in the topography and microstructure (figure 4.20b). The observed center cavities decrease the strength of the pin and they can break. Hence, the center cavities should be avoided, especially if the pins are stressed mechanically.
The element distribution mapping of the transition zone is displayed in figure 4.21. The picture shows different concentrations of Mg and Al in the base material due to the different phases. The weld zone presents a more homogeneous distribution of the elements. In the visible vicinity of the crack, no difference in element distribution is observed, which suggests they were caused by thermal contraction after solidifying. Figure 4.22 depicts the Mg and Al distribution along a path from the base material into the welding zone. A higher Al concentration is observed as the path crosses through the precipitates. In the pin zone, the main elements show a homogeneous distribution, as also observed in figure 4.22.

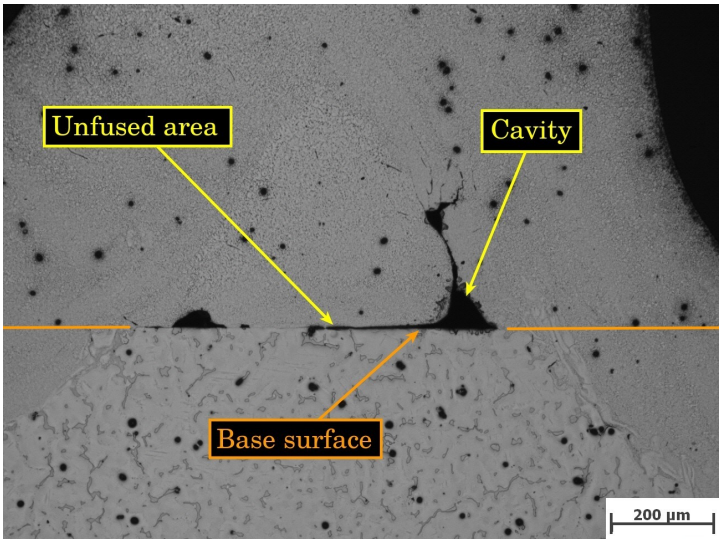

Figure 4.18: 1.5 mA pin (figure 4.19e) cavities and pin/surface interface

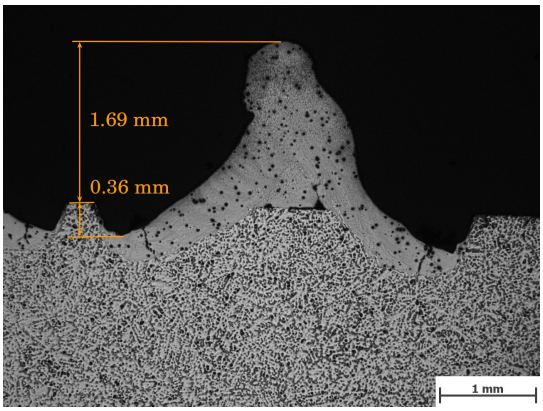

(a)

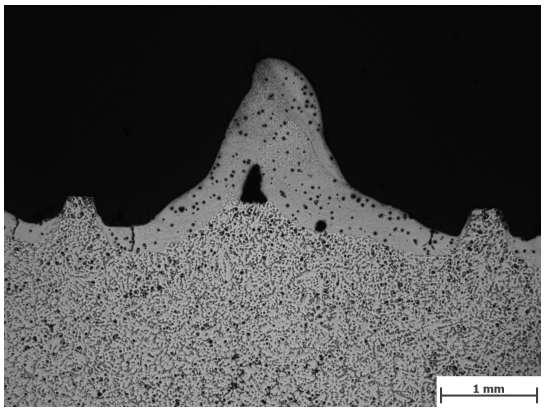

(b)

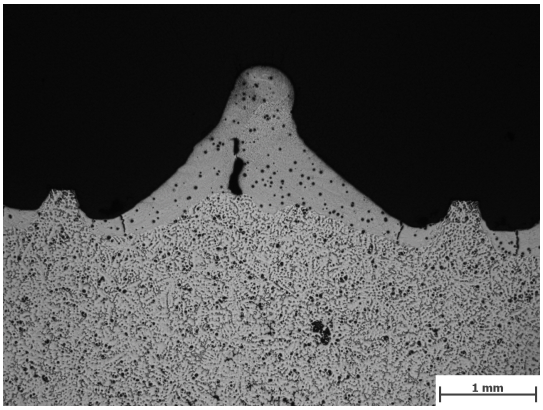

(c)

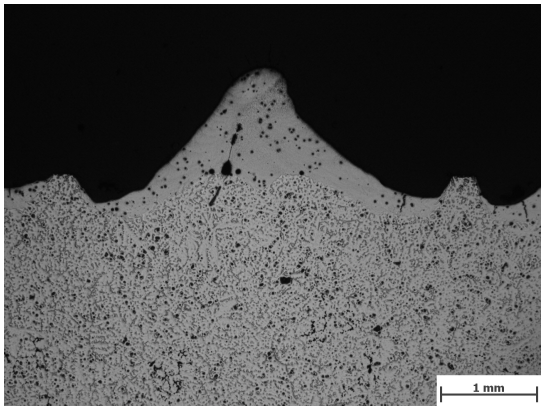

(d)

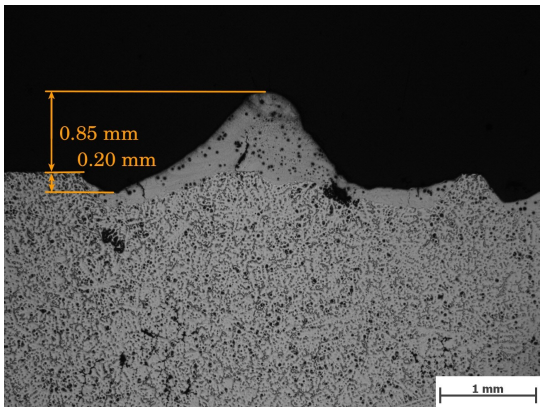

(e)

figure type	100 arm pin hexagon
array type	4x1, 16x3.46 mm
current	variable
swipes	1
time	2 s

(f)

Figure 4.19: AZ91 microsections of pins with (a) 1.5, (b) 1.4, (c) 1.3, (d) 1.2, and (e) 1.1 mA beam current.(f) Weld parameters for pin structuring

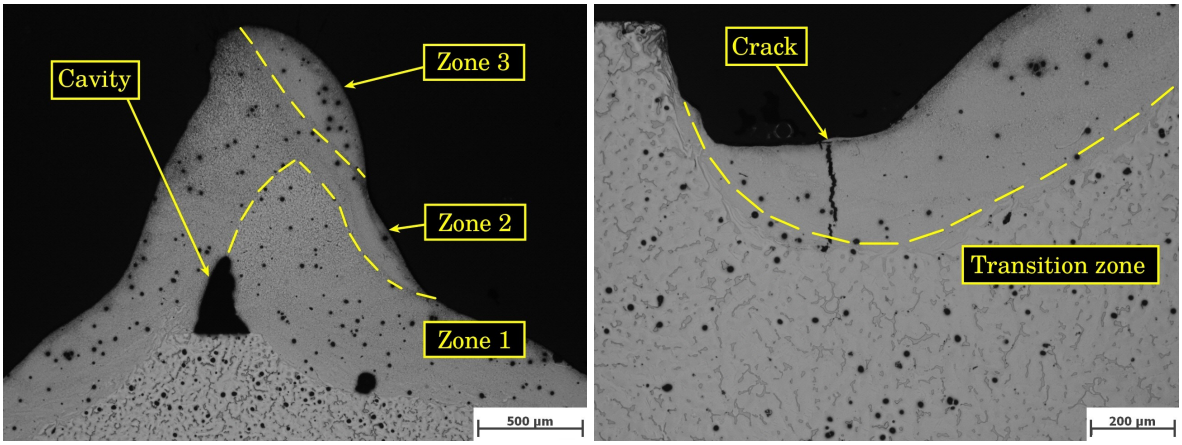

(a) (b)

Figure 4.20: 1.4 mA pin (figure 4.19d), (a) different areas and (b) pin bottom with thermocrack

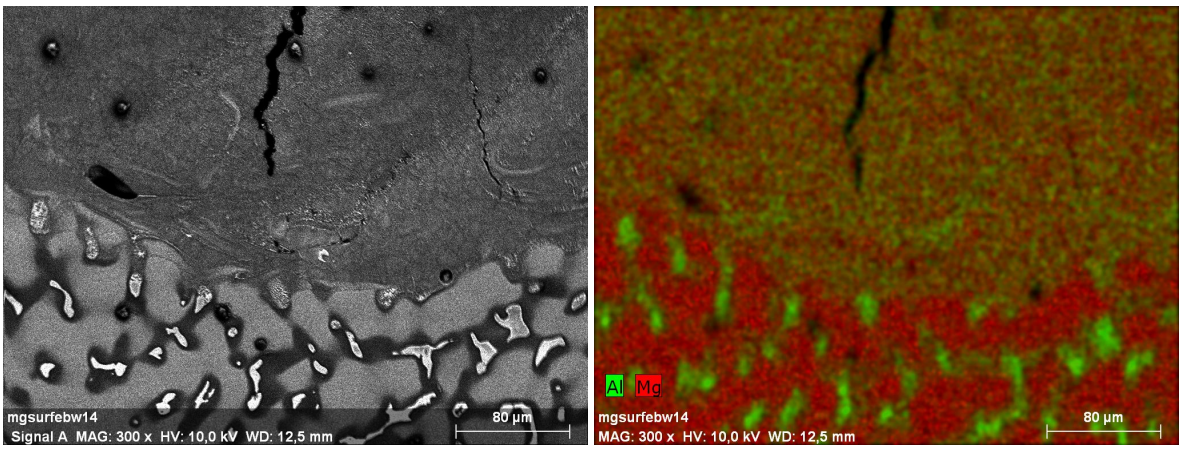

(a) (b)

Figure 4.21: AZ91 transition zone: (a) SEM image and (b) EDX mapping of the element distribution: Mg (red) and Al (green)

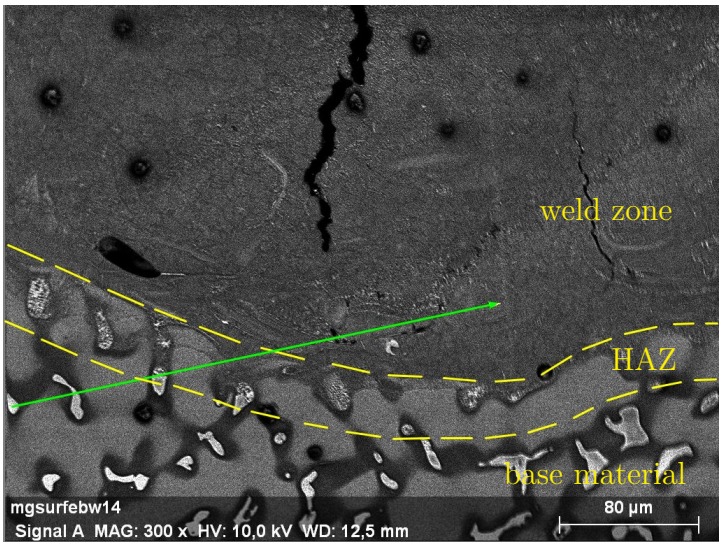

(a)

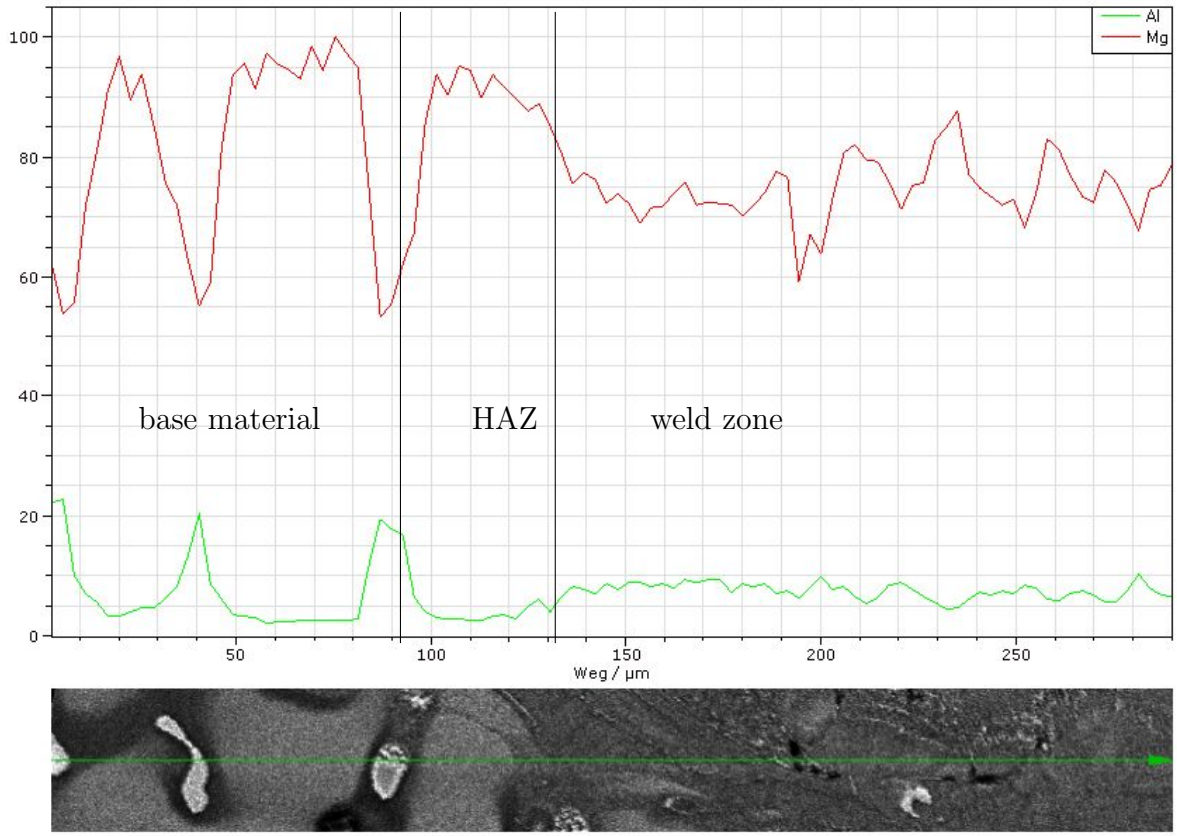

(b)

Figure 4.22: (a) AZ91 line scan from base material to weld zone, (b) chemical composition variation of Mg (red) and Al (green)

The metallography of pure Mg pins (figure 4.24) showed, that the structuring process lead to inhomogeneous pins. Figure 4.23a and 4.24d both show pins created by the same parameters, but with slightly different cross section positions. Fine grains in the pin structure were observed, with increasing grain diameter towards the pin head, as the cooling rates of the heads were lower than in the vicinity of the base material. In both materials, cavities developed in the center of the pin.

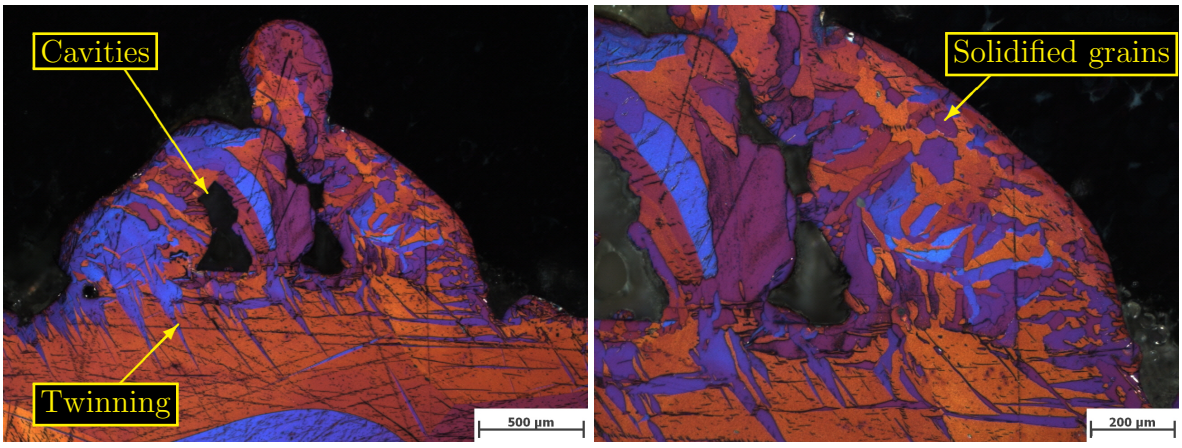

(a) (b)

Figure 4.23: (a) Microstructure of a pure Mg pin structure (1.6 mA, 1 swipe, 1 s) and (b) detailed view

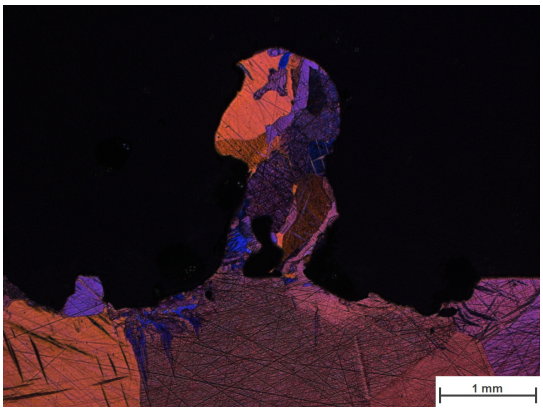

(a)

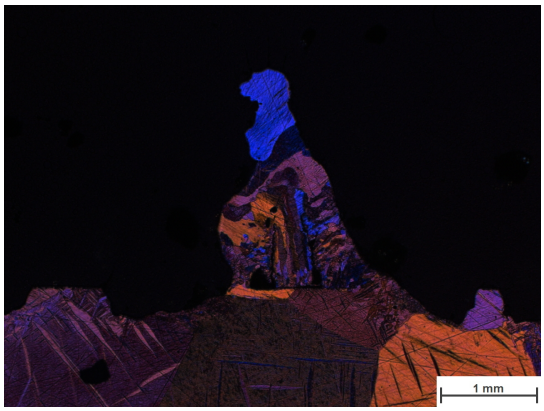

(b)

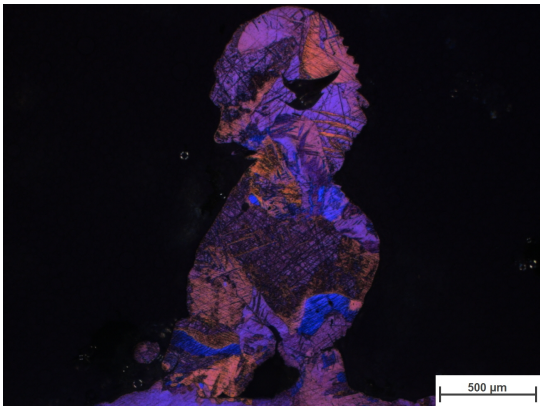

(c)

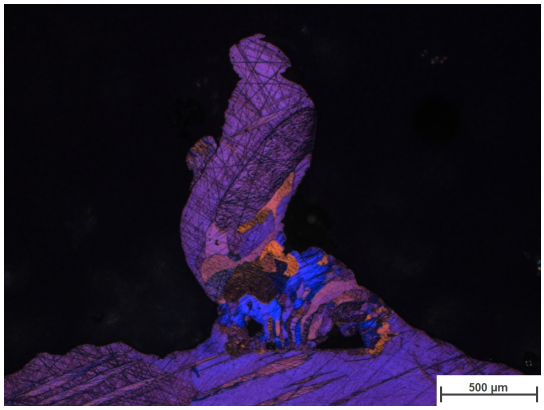

(d)

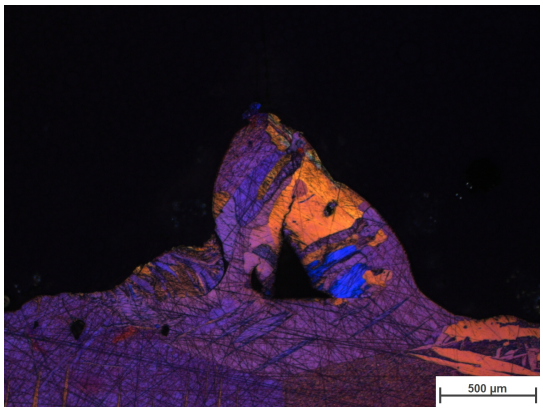

(e)

figure type	100 arm pin hexagon
array type	4x1, 16x3.46 mm
current	variable
swipes	1
time	2 s

(f)

Figure 4.24: Pure Mg microsections of pins with (a) 1.9, (b) 1.8, (c) 1.7, (d) 1.6, and (e) 1.5 mA, with (f) weld parameters

The ocurring center cavities and lack of fusion at the interfaces between pin and base surface (figures 4.20, 4.18 (AZ91), and 4.23 (pure Mg)) were a result of an insufficient melting of the center area. The problem was, that after some molten material was spilled over the edges of the weld pool, the electron beam was absorbed by the protrusion, preventing a further melting of the base material. Figure 4.25 drafts the principle of the problem. The centerline of the structure (black dashed) and electron beam (orange) are indicated. At shorter pins, the cavities were smaller.

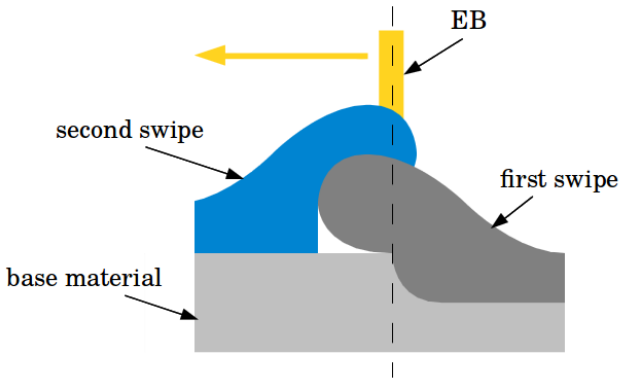

Figure 4.25: Illustration of the center spill and cavity development

4.3.5 Surface Film

During the structuring, a surface film was formed at the surface of the specimen (figure 4.26) The SEM image in figure 4.27 of the surface shows, that crystals had formed on the surface. The grooves from the sample's grinding preparation were also observed.

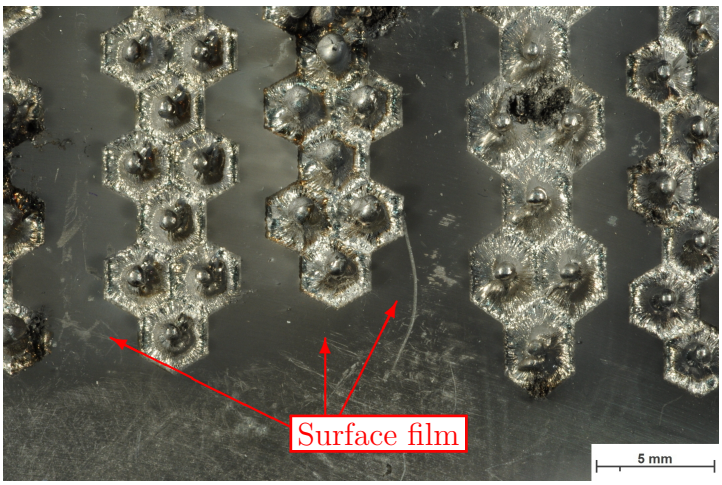

Figure 4.26: Surface film formed during structuring, visible at the surface between the pin arrays

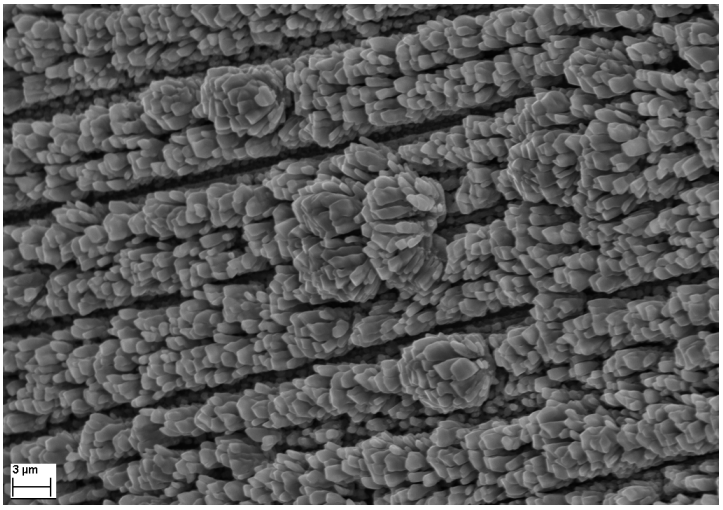

Figure 4.27: SEM image of the surface film

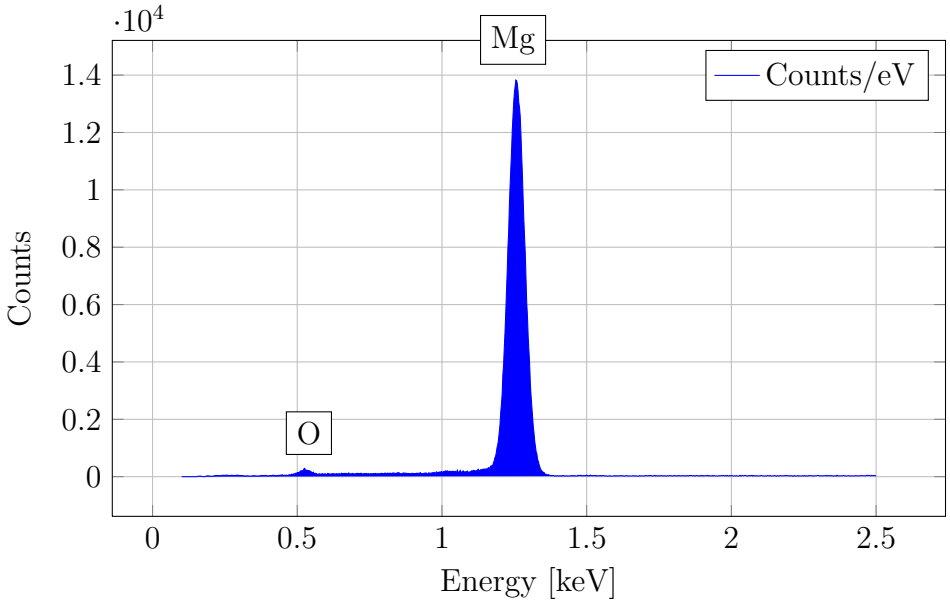

Figure 4.28: EDX total counts per energy of surface area shown in figures

EDX analysis of the surfaces (figure 4.28) confirmed a magnesium-oxygen composition. The interpretation was, that the magnesium, which vaporized during the weld process re-solidified and oxidized at the surface. Reasons for this could be the remaining oxygen in the chamber, or traces of grease on the surface.

4.4 Structure Geometry and Beam Deflection

4.4.1 Pin Perimeter and Point Spacing

The magnitude of a single protrusion arm depends on the intensity of the beam. Therefore, a slower moving beam will result in a higher protrusion, due to the higher concentration of energy, thus a bigger weld pool. The difference in the arm lengths within a figure, the larger the difference in the size of the protrusion. This leads to a concentration of bigger protrusions in the vicinity of shorter arms, as shown in picture 4.29, where three shoulders have been formed. In order to get more homogeneous pin shoulders, the deflection coordinates were adjusted to equal distances between the coordinate points, as designed previously in subsection 3.3. The resulting structure features pin slopes with shoulders towards the corners of the triangles, as depicted in figure 4.30.
Both structure arrays (figures 4.29 and 4.30) were produced using the same weld parameters. The constant travel speed can only partially compensate the difference in arm lengths, slightly inhomogeneous pin slopes are still observed. It is due to the amount of material shifted, depending on the arm length.
The difference in arm lengths decreases with increasing polygon order (the closer it gets to a circle). For a hexagon, the difference is $\cos 30° \approx 0.866$, meaning about 13% difference in arm length.

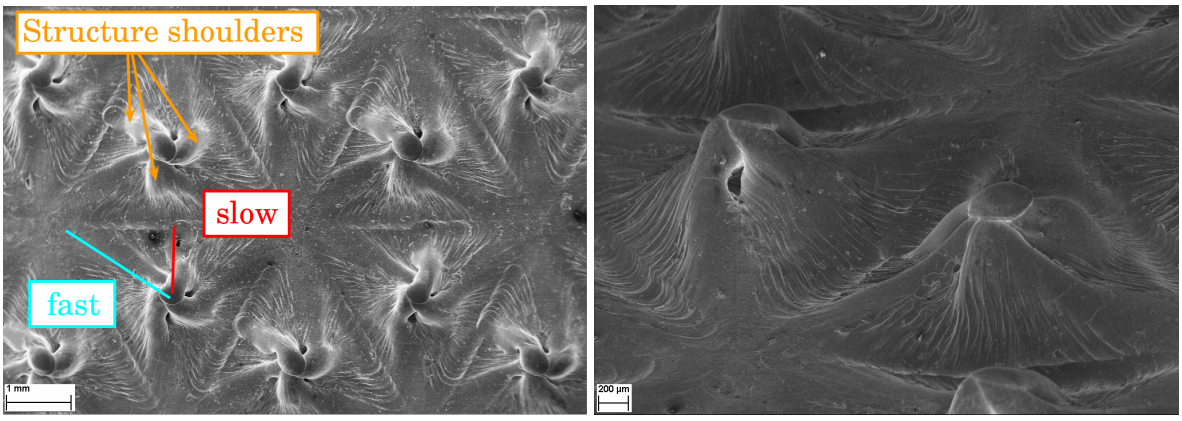

(a) (b)

Figure 4.29: SEM images of triangular structure array (99 arms, 7x3, 16x10.39mm, 1.9 mA, 1 swipe, 2 s) with annotated travel speeds, (a) top view and (b) topography of structures on AZ91

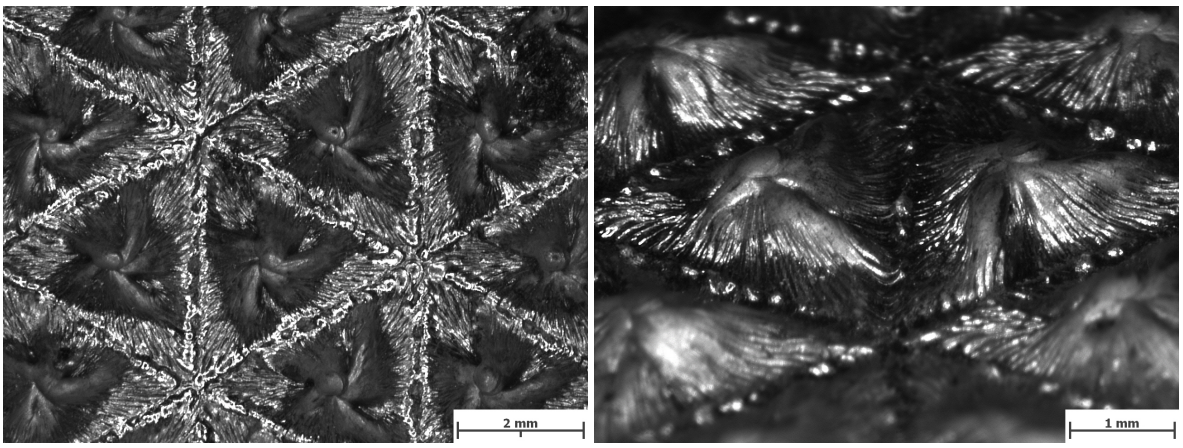

(a) (b)

Figure 4.30: LOM pictures of triangular structure array (99 arms, 16x10.39 mm, 1.9 mA, 1 swipe, 2 s) with equal point spacing, (a) top view and (b) topography of structures

4.4.2 Arm Number

Figure 4.31 compares a 100 arm and a 300 arm pin structure. With a higher number of arms the general pin topography did not change, but the surface became less rough. As the beam swipes every arm consecutively, the adjoining welding beads were overlapped. A higher number of arms means, the arms and therefore the beads are aligned closer to each other. If the dimensions of the structure are changed, it is advisable to increase or decrease the arm number accordingly, to keep a constant distance between the arm end points. Smaller structures require fewer arms, as illustrated in figure 4.32. In the present experiments, 4 mm structures with arms from 60 to 300 arms yielded acceptable results, which accounts to 0.2-0.04 mm arm end distance.

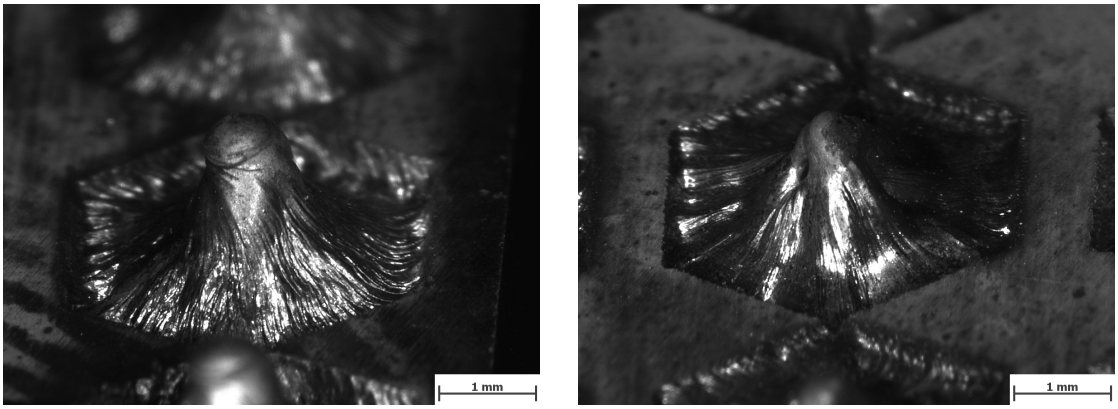

(a) (b)

Figure 4.31: (a) 100 and (b) 300 arm structure on AZ91

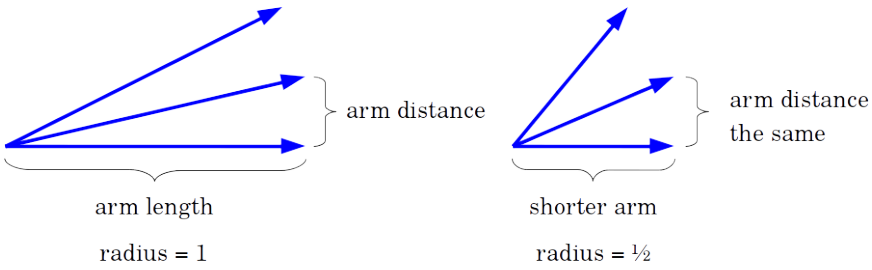

Figure 4.32: Arm distance in relation to different arm lengths

4.4.3 Limitations of Arm Number, Array Size, and Coordinate Point Distribution

Creating structures simultaneously by structure arrays promotes the structuring process by distributing the input power to multiple locations. In a structure array, the beam travels one arm per structured feature successively, leaving time for the single weld beads to cool down.The total programmable coordinate point amount is limited by the memory of the EBW machine NC (overflow at 250,000 coordinate points), thus limiting the size of the files.
For example, a figure of 40,000 points, a 3x3 array of 300 arm structures leaves $40{,}000/(3 \cdot 3 \cdot 300) = 14.81 \approx 14$ coordinate points per single arm. If the arm has only 14 points, the welding beam spends a short time at each arm to induce enough energy for the material shift. Additionally, the electron beam it is not interrupted when it shifts from arm to arm. At a low points per arm number, this energy scatter becomes noticeable. Figure 4.33 illustrates the point per arm distribution of different arm numbers with the same total point amount of 3,300.
At a 3x3 array, no sculpturing process takes place. If the total point amount is kept constant, but the size of the array is decreased to a 4x1 array, more coordinate points per arm can be obtained, which makes structures with 300 arms producible, as shown in figure 4.34. For the design of a structure, it is important to create arms with at least 30 coordinate points.

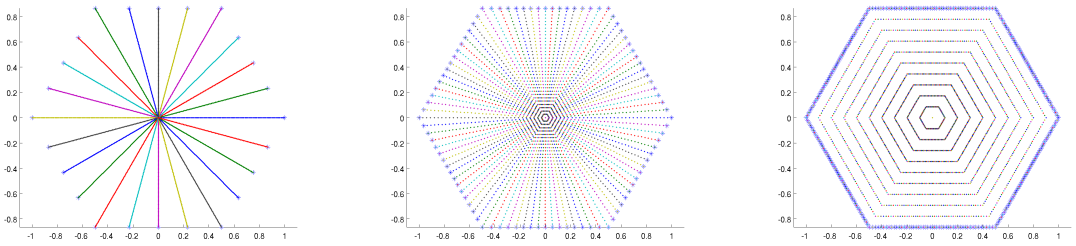

(a) (b) (c)

Figure 4.33: Coordinate point distribution of (a) 24 arm, (b) 100 arm, and (c) 300 arm structures with the same amount of points (3300)

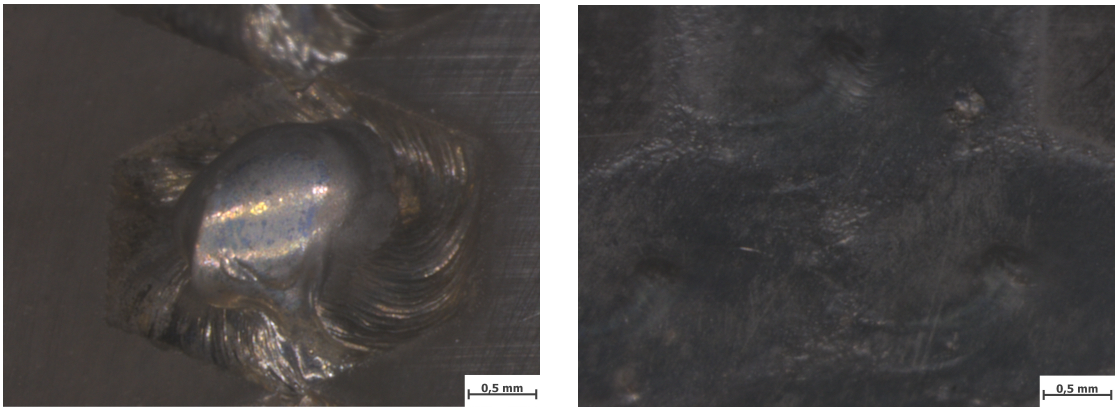

(a) (b)

Figure 4.34: Detail of 300 arm structures produced in (a) a 4x1 array and (b) a 3x3 array on AZ91

4.4.4 Arm Overlap

The overlap of the arms was intended to prevent the formation of pin cavities by concentrating the input energy to the center of the structure. Figure 4.35 shows the topographies of a non-overlapping structure (a) and an overlapping one of 15% (b) on AZ91. It can be observed, that the overlap structure features a slightly lower pin height, but a more spherical pin head. The metallography depicted in figure 4.36 showed a flawless pin body.
The results of the overlap experiments carried out on pure Mg are observed in figure 4.37. In this parameter constellation, the regular structure (a) showed an irregular pin center with cavities on the outside. The overlapping structure (b) developed a distinctive center protrusion, but cavities were observed. Overlapping on pure Mg improves the beam body's integrity. On the other hand, the elevated beam power leads to a necking of the pins, as observed in figure 4.38b.
Overlapping helped to prevent cavities partially, overlaps of up to 15% delivered the

best results with the fewest cavities, on the investigated samples of AZ91 and pure Mg. On AZ91, the overlap could go up to 25%.

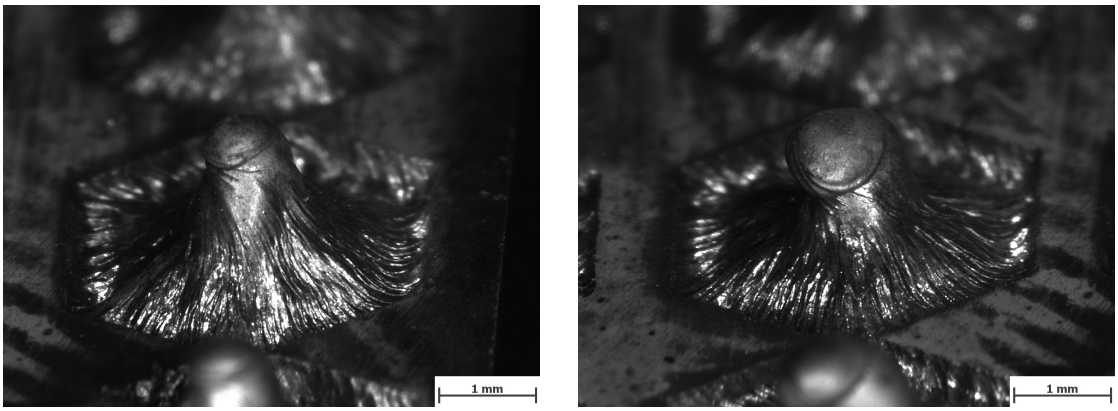

(a) (b)

Figure 4.35: LOM image of AZ91: Comparison of a (a) non-overlap with a (b) 15% overlap structure (100 arm hexagonal pins, 4x1 arrays, 16x3.46 mm, 1.5 mA, 2 s, 1 swipe)

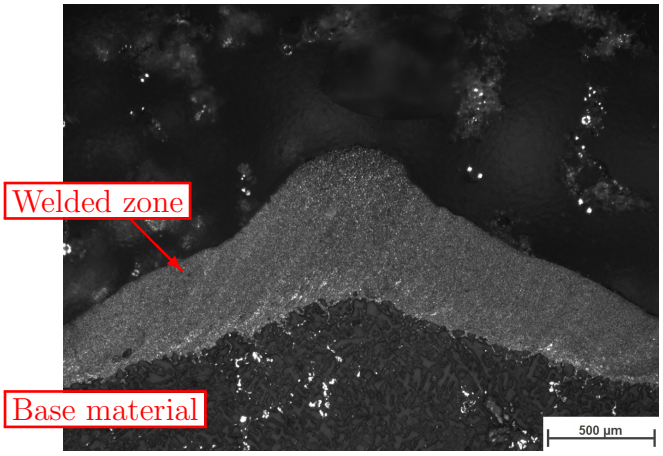

Figure 4.36: LOM image of AZ91, metallographic cross-section of 15% overlapping pin

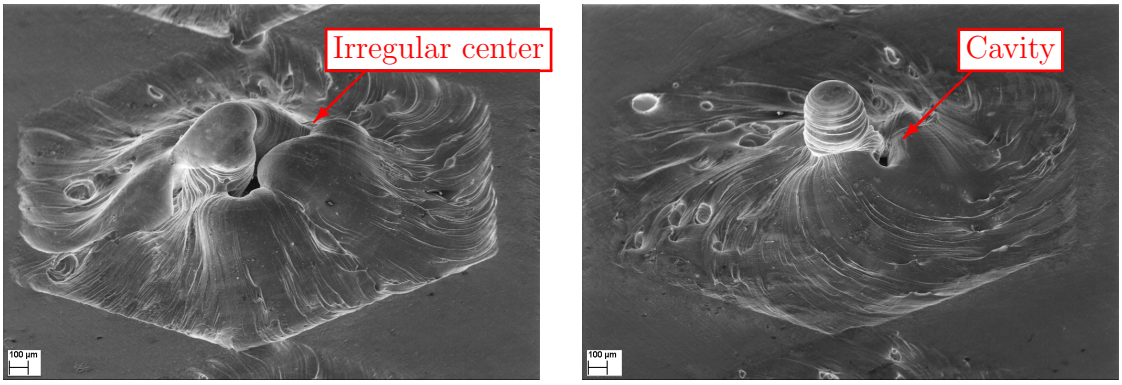

(a) (b)

Figure 4.37: SEM image of pins on pure Mg (300 arms, 4x1 array, 12x2.6 mm, 1.6 mA, 1 swipe, 2 s), (a) straight arms, and (b) with 90° counterclockwise spiral and 15% overlap

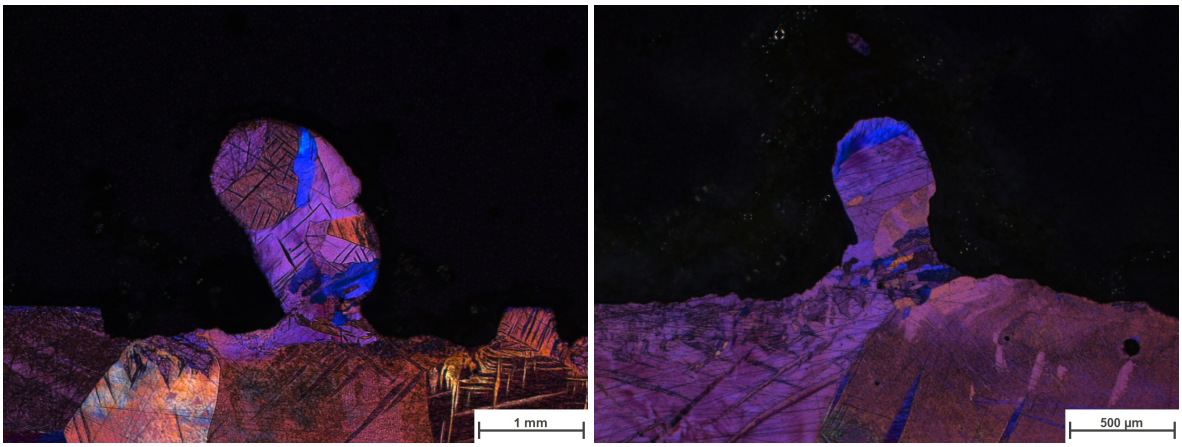

(a) (b)

Figure 4.38: Microsections of pure Mg 15% overlapping pins (100 arms, 4x1, 16x3.46 mm, 1 swipe, 2 s) (a) 1.8 mA and (b) 1.5 mA

4.4.5 Spiral Arms

The effects of spiral structures were similar on AZ91 and pure Mg. Curved structure arms resulted in a further beam travel distance, and influenced the general pin topography towards a thinner and steeper pin slope in comparison to as straight arm star structure (figures 4.39 and 4.40). Inhomogeneities at the surface were similar to structures with straight arms. Forward and backward spirals showed no difference in the resulting structures, (figure 4.41), but the spiral angle determined the pronounced shape of the pin. An effect of spiral structuring was not found in the microstructure of the pin.
Spiral structures formed a more compact pin center with a steeper pin slope, because the beam's single protrusions are stacked closer together by the curved beam paths. A 90° spiral angle delivered the best results, in case the pins worked as mechanical interlocks, where an angular pin slope would provoke a sliding between the joined parts.

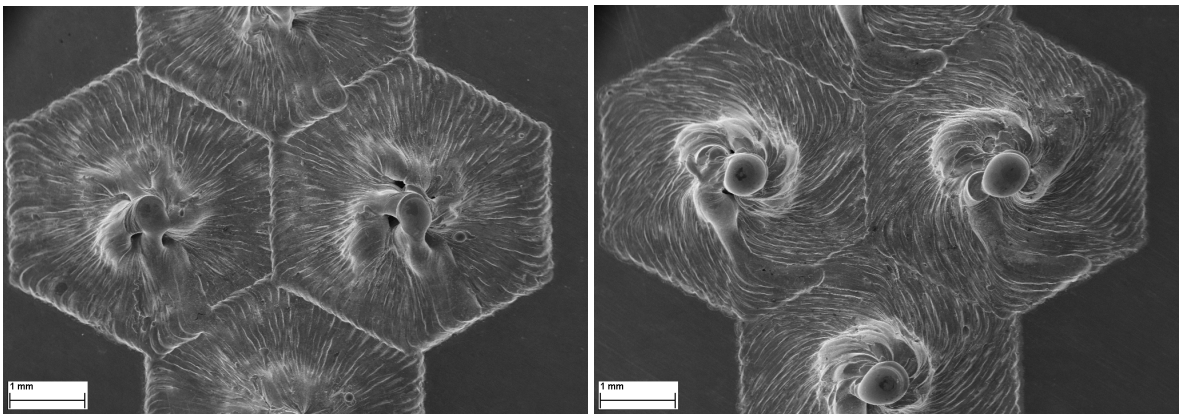

(a) (b)

Figure 4.39: SEM image of top view of (a) a hexagonal star structure compared to (b) a spiral structure

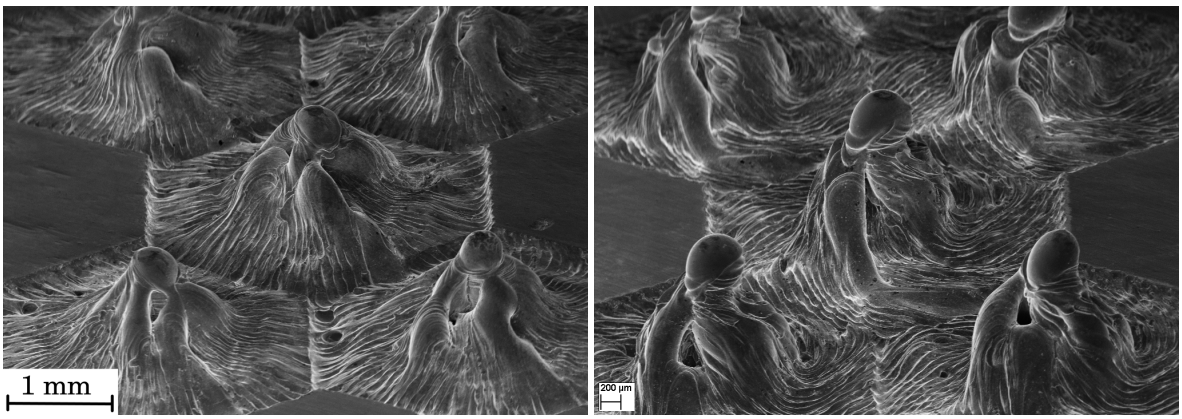

(a) (b)

Figure 4.40: SEM image of topography of (a) hexagonal star structures compared to (b) spiral structures on AZ91 (60 arm hexagons, 90° forward spiral, 3x3 array, 19x6.92 mm, 1.6 mA, 1 swipe, 1 s)

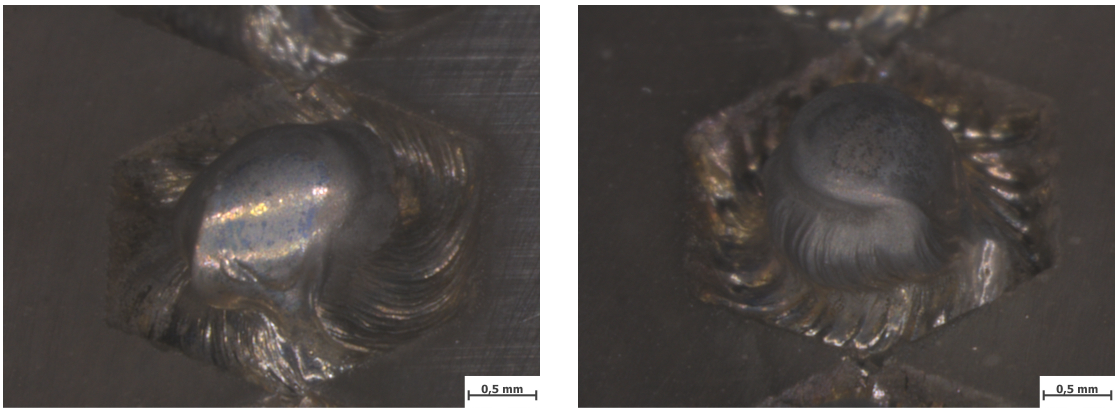

(a) (b)

Figure 4.41: LOM image of topography of (a) 90° counterclockwise spiral and (b) 90° clockwise spiral, with 25% overlap on AZ91

4.4.6 Beam Travel Direction

An inversed beam travel direction resulted in surface intrusions ("walls"). Figure 4.42 shows a triangular structure array with produced intrusions, in comparison to a pin structure array (figure 4.30). For plain surface modification without pins, a wall structure is more suitable, as the material from the structuring process is redistributed along the perimeters of the structures, rather than concentrated at the center points. This results in a more homogeneous topography.

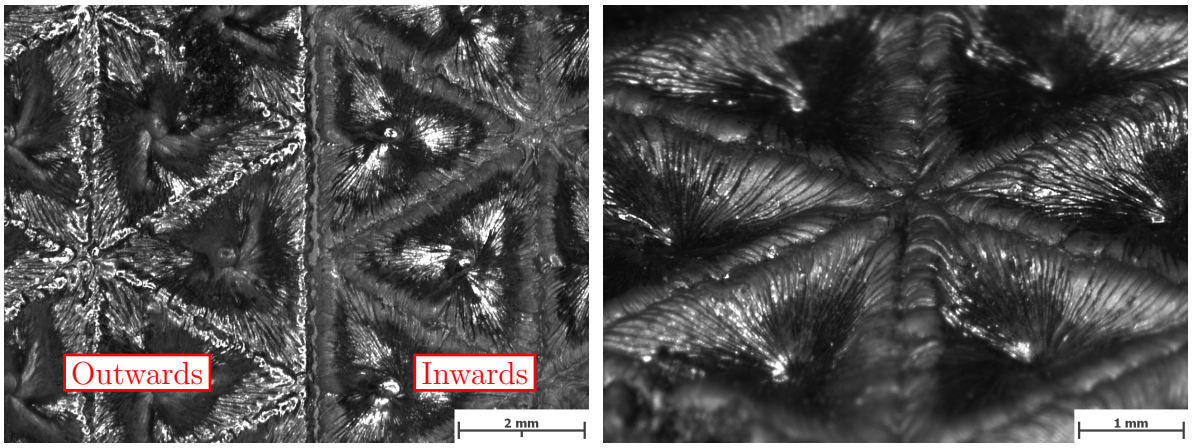

(a) (b)

Figure 4.42: LOM image of inward structure on AZ91 (99 arm triangles, 7x3 array, 16x10.39 mm, 1.9 mA, 1 swipe, 2s), (a) top view, bordering on outward array (pins, left) and (b) topography of intrusions

4.4.7 Array Combination

As described in section 3.3, 6-arm hexagon arrays ("flakes") were used in micro-figures with small structure dimensions. Figure 4.43 shows a flake array with 4 mm pin diameter. Here, the space between the branches of the structures remains unaffected. This remaining space was filled with an array of triangles. The result of these two consecutive structuring processes is shown in figure 4.44. The array combination fills the entire area, with smaller pins aligned between the base flake array.

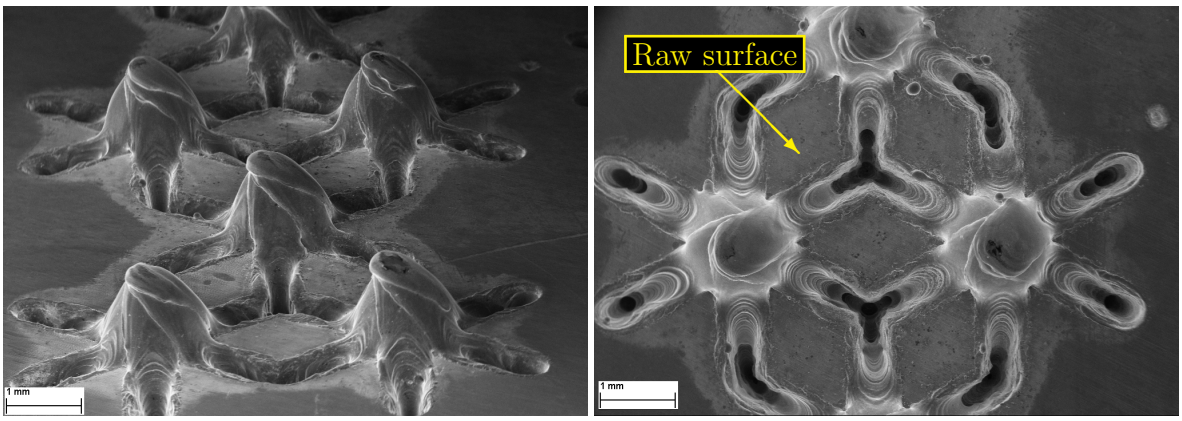

(a) (b)

Figure 4.43: (a) 3x3 flake array on AZ91 with (b) top view

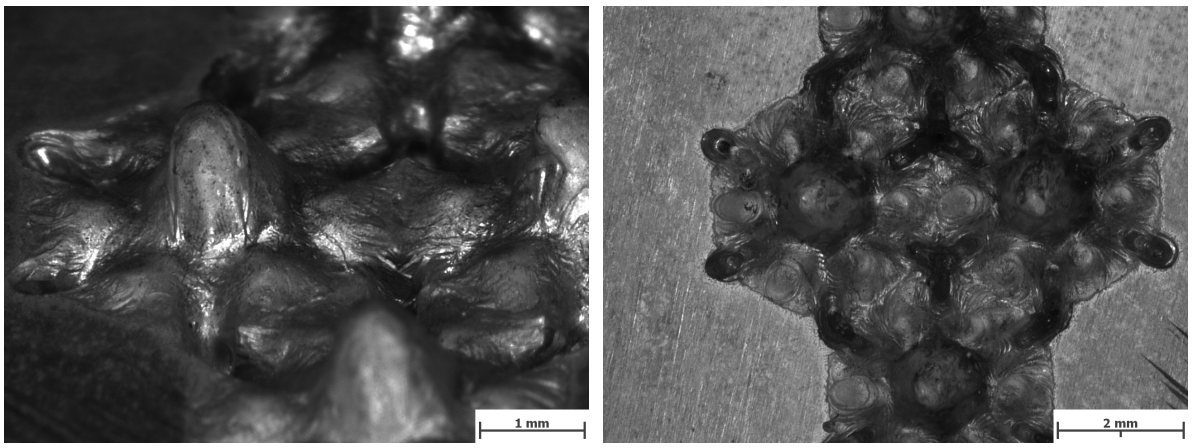

(a) (b)

Figure 4.44: (a) Flake array (3x3, 19x6.92 mm) filled with triangles (30 arms each, 1.1 mA, 1 swipe, 2 s) and (b) top view (AZ91)

4.4.8 Swipe Number

Figure 4.45 compares a hexagonal pin created with a single swipe to a two swipe exemplar, both on AZ91. The pin's slope became smoother with an increasing number of swipes. The cross-section in figure 4.46 shows two structures on top of each other, caused by the two swipes, the second swipe causing a secondary cavity.
On pure Mg, a structuring process with two swipes in two seconds resulted only in a surface roughening, but a pin creation did not occur (figure 4.47). With the beam traveling at double the speed, the single beam swipes induced too little energy into the surface to evoke protrusions.
Finally, it was observed, that multiple beam swipes on AZ91 did not improve the pins' properties, while for pure Mg, multiple swipes eliminated the pin creation.

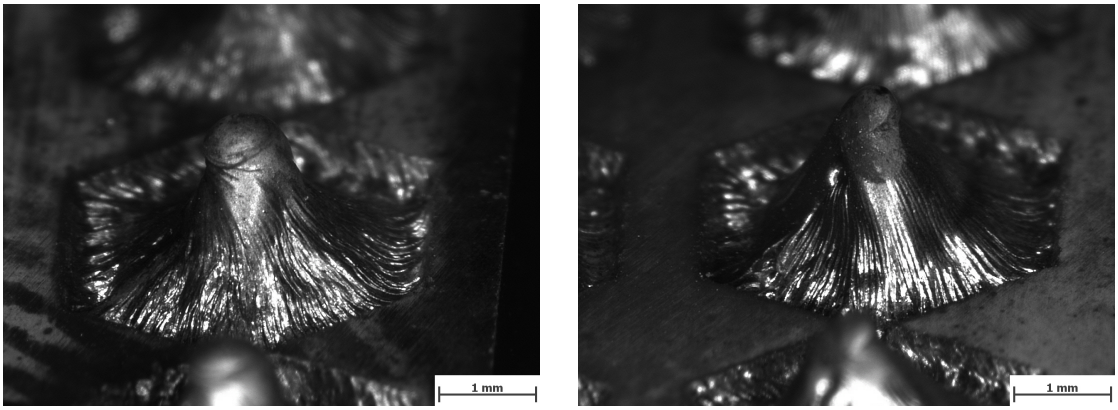

(a) (b)

Figure 4.45: Pins on AZ91 (100 arms, 4x1 arrays, 16x3.46 mm, 1.5 mA, 2 s), created with (a) single swipe and (b) two swipes

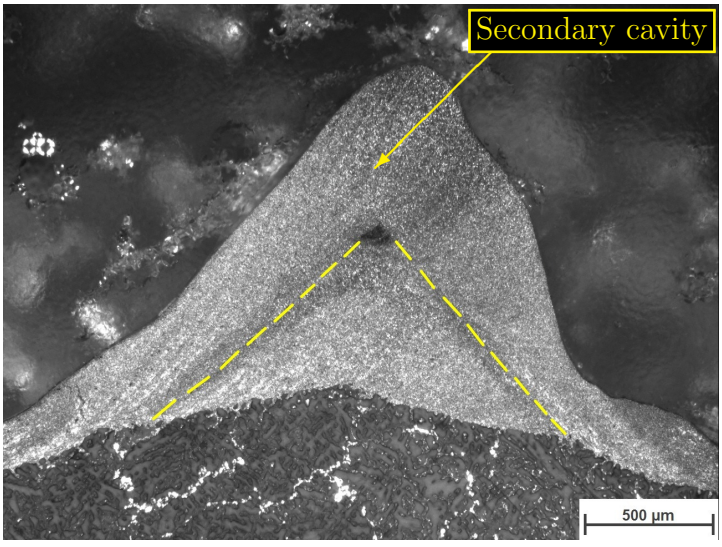

Figure 4.46: Microsection of two swipe pin, with visible secondary cavity (LOM, AZ91)

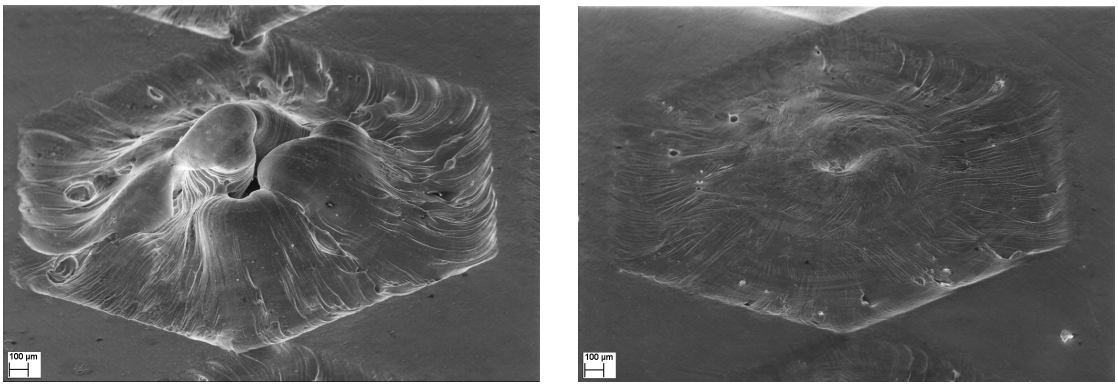

(a) (b)

Figure 4.47: Pins on pure Mg (300 arms, 12x2.6 mm, 1.6 mA, 2s), created with (a) a single swipe, and (b) two swipes (SEM)

4.4.9 Multi-step Pin Creation

Multi-step pin creations with a large variation of the beam power proved no positive aspects. Experiments were carried out swiping the surface with reduced power of the main beam current (2 mA), both prior and after the structuring process. Both processes did not influence the result, figure 4.48 compares a two-step pin to a regular structure (process parameters in table 4.3), where no particular difference is observed. It can be said, that preheating or smoothing with low power is unnecessary, at least using the parameters of table 4.3.

Table 4.3: Weld parameters of staged pin creation, as shown in figure 4.48

figure type	300 arm pin hexagon	
array type	3x3, 14.25x5.19 mm	
	stage 1	**stage 2**
arms	star	90° spiral
current	2 mA	1.6 mA
swipes	2	2
time	2 s	2 s

A sequence of three successive structuring processes with similar beam powers produced a pin structure with a very homogeneous and smooth surface, as shows figure 4.49. Table 4.4 states the according weld parameters of each stage. Between the steps the specimen was able to cool down within 10-15 seconds (schematic temperature course in figure 4.50)
The three-step pin creation improved the surface homogeneity as the structures were able to dissipate some of the heat between the steps, in contrast to swiping the structure multiple times without interruption. The variation in arm numbers of each step reduced the surface ribs observed on regular structures.

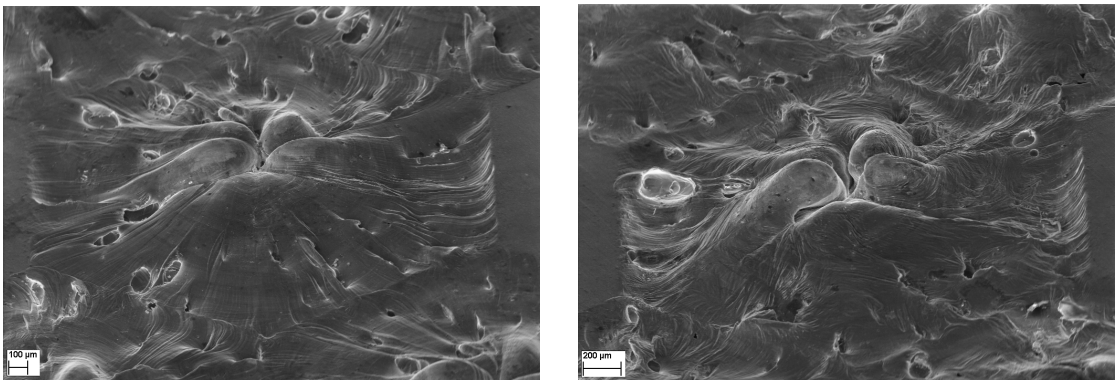

(a) (b)

Figure 4.48: Pins on pure Mg (300 arms, 14.25x5.19, 1 swipe, 1 s) (a) single step and (b) two-step (same array, 1.6 mA)

Table 4.4: Three-step pin weld parameters

	stage 1	**stage 2**	**stage 3**
figure type	300 arm	100 arm	300 arm
		pin hexagon	
array type		4x1, 16x3.46 mm	
current	1.5 mA	1.5 mA	1.5 mA
swipes	2	1	1
time	2 s	2 s	2 s

Figure 4.51 shows the microstructure of a three-step pin, where the different layers of the successive structuring processes are visible. A multi-step process made the pin erection of big protrusions more reproducible, as it prevented cavity formation. On the other hand, the roughness of the surface decreases.

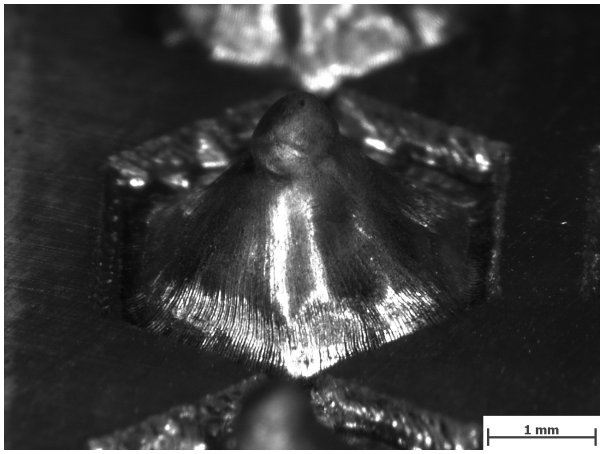

Figure 4.49: Three-step pin topography by stereo microscopy

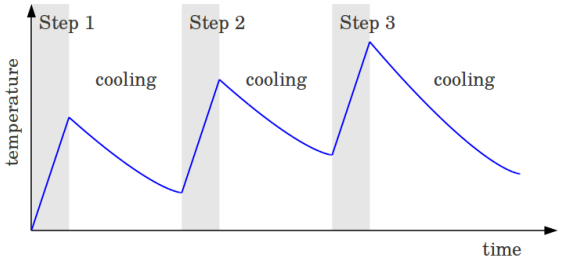

Figure 4.50: Schematic temperature course over time during three-step pin creation, with cooling time between the steps

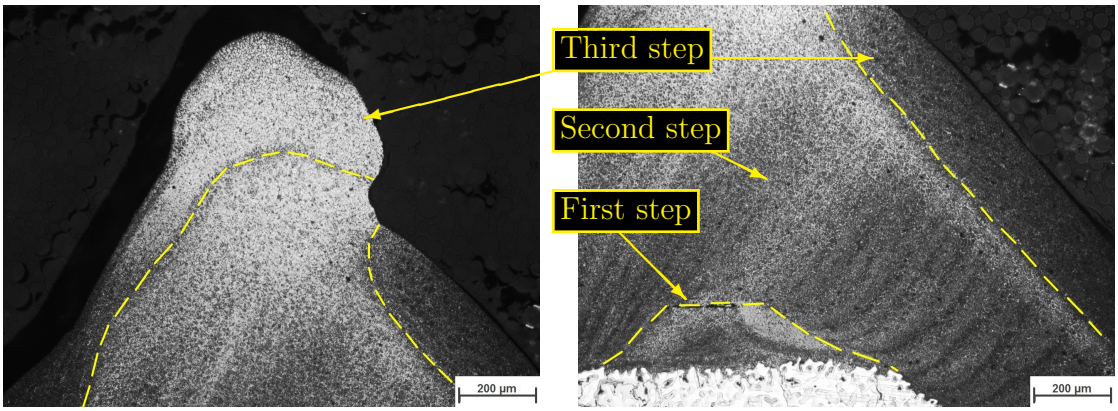

(a) (b)

Figure 4.51: Three-step pin microstructure, (a) pin head and (b) pin slope with different pin layers

4.5 Influences on Surface Roughness

4.5.1 Standard Structure

The surface roughness was mainly influenced by the arm number and the number of swipes. Figure 4.52a shows a top view of the recorded 3D data, the black areas in the picture result from light reflections, which made a height determination impossible for the software. In all analyzed structures the scanning path was set 0.5 mm parallely inwards from the perimeter of the structure, as indicated by the red line. The measured profile along this path is displayed in figure 4.52b. Applying a high-pass filter (with the cutoff of table 4.6) delivers the course of figure 4.52c, the roughness. The resulting R_a is 7.35 μm, a value comparable to rough machining [32].

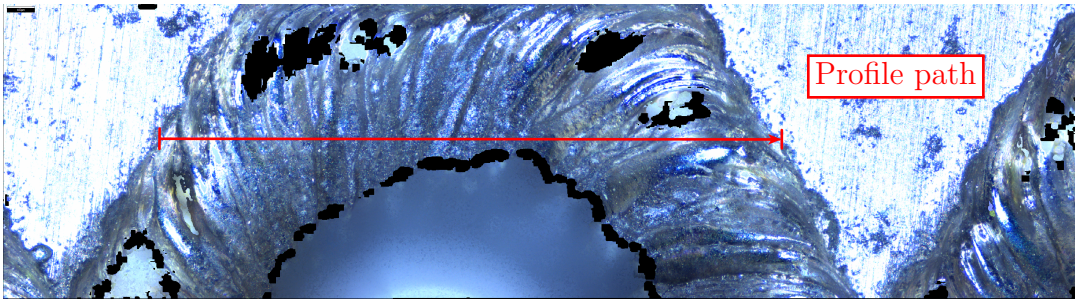

(a)

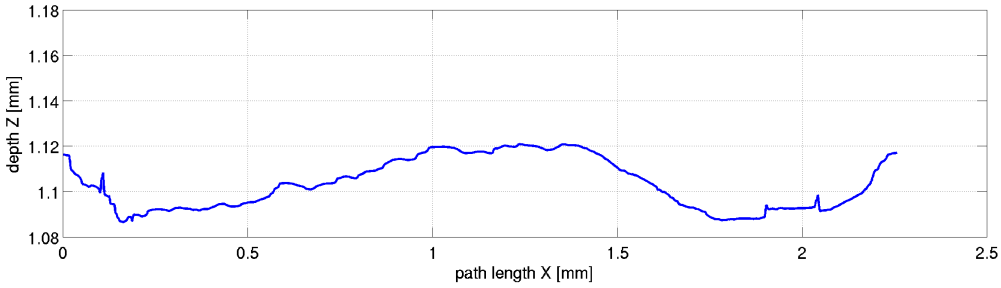

(b)

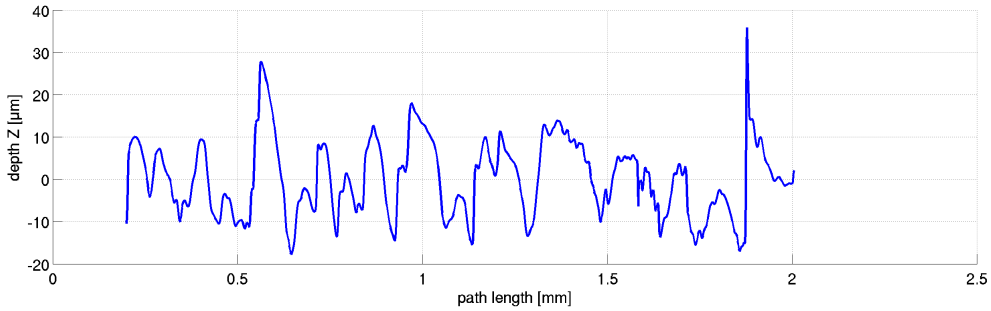

(c)

Figure 4.52: (a) Surface profile path, (b) measured primary profile, and (c) filtered roughness profile (AZ91, 100 arm hexagon, 3x3 array)

Table 4.5: Structuring parameters

figure type	100 arm hexagon pin
array type	4x1, 12x2.6 mm
current	1.6 mA
swipes	1
time	2 s

Table 4.6: Measurement values and resulting roughness

Profile length	3.44 mm
Z resolution	100 nm
Lateral res.	4 μm
Cutoff	250 μm
R_a	7.35 μm

4.5.2 Arm Number

The structure with 100 arms for AZ91 got a $R_a = 7.35$ μm, while $R_a = 2.75$ μm was measured on a 300 arm structure. To sum up, the three times closer stacked weld beads resulted in an approximate third of the R_a roughness value. When the array was extended from 4x1 to 3x3, a pin creation did not occur, as described in section 4.3.2. The modified surface of a 3x3 array (AZ91, 1.6 mA, 1 swipe, 2 s) featured a R_a of 0.72 μm.
Pure Mg structured with 300 arms, 3x3 structure array, showed also no pins, but only a surface roughness, as depicted in figure 4.53. The spike at position 400 μm is caused by an inhomogeneous peak at the surface, indicated in figure 4.53b. The calculated R_a was 2.75 μm.

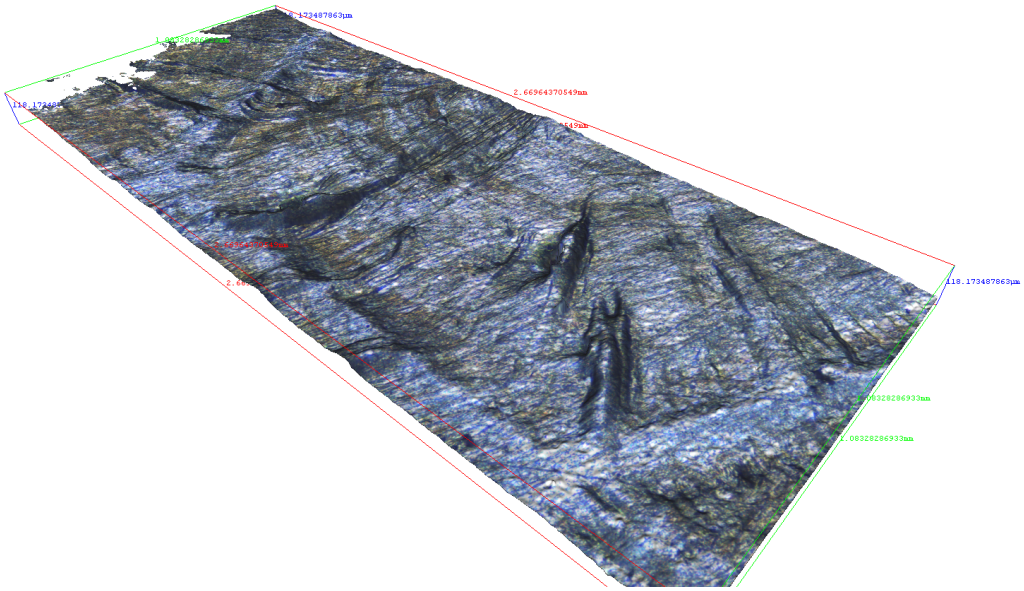

(a)

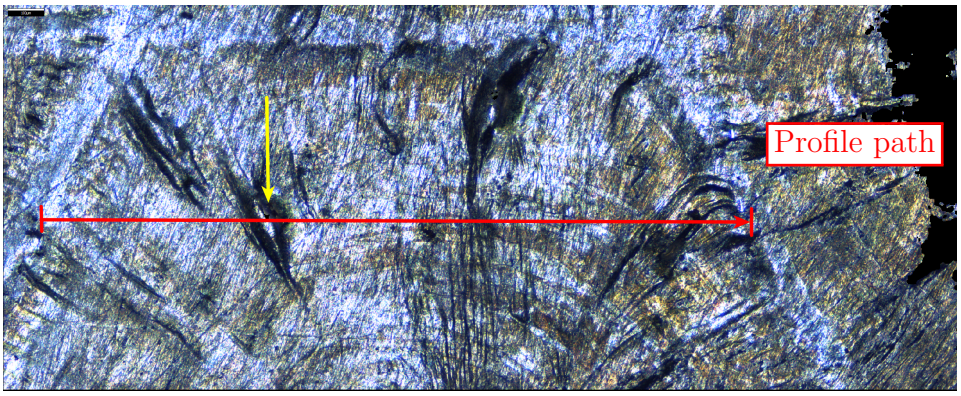

(b)

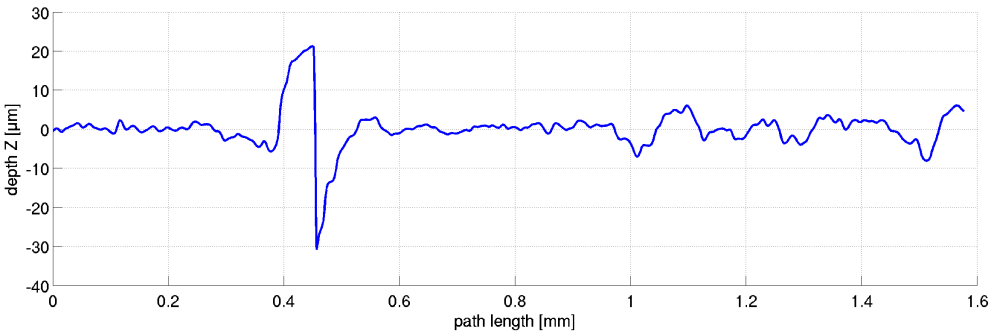

(c)

Figure 4.53: (a) *Alicona* recorded 3D profile, (b) investigated profile path, and (c) roughness profile (pure Mg, 300 arm hexagons, 3x3 array)

Comparison of Pure Mg and AZ91

With the EB surface structuring technique, R_a values from 0.7 to 8.1 were achieved in the structured areas, as listed in detail in table 4.7. Compared to AZ91, the surfaces of pure Mg are in general rougher after EBW [35].

Table 4.7: Measured roughnesses from the same linescan of different surface structures and materials

	Array	3x3	4x1
Material	Structure	R_a [μm]	
AZ91	100 arms	**8.10**	**7.35**
	300 arms	**0.72**	**2.75**
Pure Mg	100 arms	**4.14**	**-**
	300 arms	**2.75**	**7.42**
	300 arms, 2 swipes	**-**	**1.75**

5 Summary and Conclusions

A surface modification was performed on pure magnesium and magnesium alloy AZ91 by the means of an electron beam. The main objective was to obtain a structured surface, which is necessary for bioapplications (implants). The resulting surface structures were assessed by stereo microscopy and scanning electron microscopy. Surface mappings were created by an *Alicona* microscope to determine the surface roughnesses. Microstructure and microstructural changes were analyzed using light optical microscopy and EDX analysis. The results are summarized as follows:

1. Creating surface protrusions in the shape of pins was accomplished and facilitated on both pure Mg and AZ91 by programming the beam deflection of the EBW machine.

2. The beam deflection control files were created utilizing MATLAB. Scripts for creating different beam deflection structures with various parameters were written.

3. The pins were aligned in arrays of multiple single structures, produced quasi-simultaneously. The amount of the created structures required an adjustment of the beam power, as the input energy is maintained on the same level.

4. The resulting surface features were influenced by a combination of deflection figure, beam power, and deflection speed. Depending on the dimensions of the structure, the deflection figure must be adapted (arm number, coordinate point distribution)

5. The achieved pin height was linked to the input energy per covered area. Pin heights of 2 mm (AZ91) and 2.5 mm (pure Mg) with 4 mm pin diameter were produced with 14 $^{J}/_{mm^2}$. Pure Mg showed a higher increase in pin height with increasing input energy.

6. Pin shapes were additionally produced using curved beam swipes, which resulted in a steeper pin slope. Overlapping arms formed spherical pin heads.

7. Especially the multi-step process produced pins with no internal defects and has a large potential due to the combination of the cooling rate and figures.

8. Pure Mg formed column-like pins with large inhomogeneities and defects in the pin-base material interface. Pin structures on pure Mg were less reproducible than AZ91 pins. Cracks were observed on the pin surface of both pure Mg and AZ91, resulting from thermal contraction during solidification.

9. Increasing the arm number, multiple swipes, and multi-step pin creation smoothened the surface of the pins and decreased the surface roughness. Roughness values R_a from 0.72 to 8.10 were achieved. Pure Mg showed rougher surfaces than AZ91, due to its different welding behavior. Pure Mg possesses a lower surface tension, which is crucial for the surface structuring process.

10. On pure Mg, metallography analysis showed fine grains in the produced surface structures. Macroscopic cavities in the pins, resulting from the sculpturing process, could not be avoided entirely, but were less developed at overlapping structures and at smaller structures.

11. The microstructural layout of AZ91 (α-Mg, massive γ-, and lamellar (α+γ)-precipitates) was refined in the melt zone, while Mg and Al were re-distributed more evenly by the structuring process. A small HAZ developed adjacently to the pin structures, where the phases melted and re-solidified in an eutectic (α+γ)-phase. Cavities in AZ91 could be suppressed by dividing the sculpturing process into two or three steps. Furthermore, overlapping structures showed also smaller cavities.

Conclusions

The EB structuring process depends not only on the combination of many physical properties from the material, like the surface tension of the melt, the melting range, and heat conductivity of the material, but also on the EBW equipment. The machine specifications limit the achievable beam focus, which limits the size of the surface structures. The number of quasi-simultaneously producible pin structures depends on the heat dissipation and also on the amount of programmable coordinate points, which is limited by the memory of the machine.
To create pin structures, the energy input has to be adjusted to the array size and the figure diameter. In pure Mg and AZ91, structures with 100 arms are reproducible in a range of pin diameters from 2 mm to 5 mm, with an energy input per area from 5 to 14 $^{J}/_{mm^2}$ in AZ91 and from 8 to 14 $^{J}/_{mm^2}$ in pure Mg. The arm number can be increased to obtain a smoother surface, or lowered for a rougher surface. To avoid cracks and cavities, using a multi-step pin creation or an overlapping structure is recommended.
Research has shown influence of surface roughnesses from R_a = 0.03-1.5 μm of Ti-alloys on cell adherence and alignment [37], which makes the achievable surface roughnesses by EB structuring suitable for bioapplications.

Outlook

EB treated test samples of pure Mg and AZ91 must be subjected to tests *in vitro* and *in vivo*, to evaluate their behavior in active and living environments. After the results of these tests, the structuring process can be adjusted accordingly.
The change of the surface by topographical modification could also be combined with another method to create a roughness for cell adherence.

In this work, the voltage was not changed. If the voltage is lowered, the beam current must be increased to maintain the same energy input. A higher current means, that the power can be adjusted finer.
The roughness value R_a was used throughout this work, because it allows an easy comparison between different structures, using only a single value. However, because of the statistical nature of R_a, it represents only a part of the roughness information. To improve the analysis, additional processing of the raw data is necessary. An example could be an area scan (3D analysis).
The EB surface structuring of other biomaterials TiAl6V4 and AZ31 is planned as well. AZ31 has similar properties like AZ91, therefore a similar structuring effect is expected. For TiAl6V4, a higher energy input will have to be provided, due to the higher heat capacity and melting enthalpy of the Ti-alloy.

Bibliography

[1] Buddy D. Ratner, Allan S. Hoffman, F. I. Schoen, and Jack E. Lemons. *Biomaterials science: an introduction to materials in medicine.* Cambridge Univ Press, 3rd edition, 2004.

[2] David F. Williams. *Definitions in biomaterials: proceedings of a consensus conference of the European Society for Biomaterials, Chester, England, March 3-5, 1986*, volume 4. Elsevier Science Ltd, 1987.

[3] J.Y. Wong and J.D. Bronzino. *Biomaterials.* Taylor & Francis, 2007.

[4] Xue-Nan Gu and Yu-Feng Zheng. A review on magnesium alloys as biodegradable materials. *Frontiers of Materials Science in China*, 4(2):111–115, 2010.

[5] Sarah E. Henderson, Konstantinos Verdelis, Spandan Maiti, Siladitya Pal, William L. Chung, Da-Tren Chou, Prashant N. Kumta, and Alejandro J. Almarza. Magnesium alloys as a biomaterial for degradable craniofacial screws. *Acta Biomaterialia*, 10(5):2323–2332, 2013.

[6] Guangling Song. Control of biodegradation of biocompatable magnesium alloys. *Corrosion Science*, 49(4):1696–1701, 2007.

[7] Y.F. Zheng, X.N. Gu, and F. Witte. Biodegradable metals. *Materials Science and Engineering: R: Reports*, 77(0):1–34, 2014.

[8] Otto Helmboldt, L. Keith Hudson, Chanakya Misra, Karl Wefers, Wolfgang Heck, Hans Stark, Max Danner, and Norbert Rösch. *Aluminum Compounds, Inorganic.* Wiley-VCH Verlag GmbH & Co. KGaA, 2000.

[9] A. Srinivasan, J. Swaminathan, M.K. Gunjan, U.T.S. Pillai, and B.C. Pai. Effect of intermetallic phases on the creep behavior of AZ91 magnesium alloy. *Materials Science and Engineering: A*, 527(6):1395–1403, 2010.

[10] Adolf Beck. *Magnesium und seine Legierungen.* Springer, 2 edition, 2001.

[11] K.N. Braszczyńska-Malik. Spherical shape of γ-Mg17Al12 precipitates in AZ91 magnesium alloy processed by equal-channel angular pressing. *Journal of Alloys and Compounds*, 487(1–2):263–268, 2009.

[12] C.R. Hutchinson, J.F. Nie, and S. Gorsse. Modeling the precipitation processes and strengthening mechanisms in a Mg-Al-(Zn) AZ91 alloy. *Metallurgical and Materials Transactions A*, 36(8):2093–2105, 2005.

[13] City College of San Francisco. `http://www.ccsf.edu`, January 2014.

[14] M. Moravej, A. Purnama, M. Fiset, J. Couet, and D. Mantovani. Electroformed pure iron as a new biomaterial for degradable stents: In vitro degradation and preliminary cell viability studies. *Acta Biomaterialia*, 6(5):1843–1851, 2010.

[15] Sebastian Bauer, Patrik Schmuki, Klaus von der Mark, and Jung Park. Engineering biocompatible implant surfaces: Part I: Materials and surfaces. *Progress in Materials Science*, 58(3):261–326, 2013.

[16] R. Walter, M. Bobby Kannan, Y. He, and A. Sandham. Effect of surface roughness on the in vitro degradation behaviour of a biodegradable magnesium-based alloy. *Applied Surface Science*, 279(0):343–348, 2013.

[17] Paul Hilton and Ian Jones. A new method of laser beam induced surface modification. *The Laser User*, (51):46–48, 2008.

[18] U. Reisgen, C. Otten, H. Fischer, and C. Panfil. Electron beam structurisation of titanium materials for medical applications: potential for improved bone ingrowth beaviour. *2nd International Electron Beam Welding Conference*, 285:68–71, 2012.

[19] Z. Pu, J.C. Outeiro, A.C. Batista, O.W. Dillon Jr, D.A. Puleo, and I.S. Jawahir. Enhanced surface integrity of AZ31B Mg alloy by cryogenic machining towards improved functional performance of machined components. *International Journal of Machine Tools and Manufacture*, 56(0):17–27, 2012.

[20] Helmut Schultz. *Electron beam welding*. Elsevier, 1994.

[21] G. Schubert. Electron Beam Welding – Process, Applications and Equipment. PTR - Precision Technologies Inc., 120 Post Road, Enfield, CT 06082 USA, 2008.

[22] Bruce Dance and Anita Buxton. An introduction to Surfi-Sculpt® technology - new opportunities, new challenges. *7th International Conference on Beam Technology*, 2007.

[23] J. Tändl, L. Wittwer, and N. Enzinger. Erzeugung von Pinstrukturen mittels Elektronenstrahloberflächenbehandlung. *Schweiss- und Prüftechnik*, Sonderausgabe:32–35, 2013.

[24] Bruce Dance, Irvine Guy, Ewen Kellar, Crawford James, et al. Workpiece structure modification, April 9 2004. WO Patent 2,004,028,731.

[25] Jonathan Blackburn and Paul Hilton. Producing Surface Features with a 200 W Yb-fibre Laser and the Surfi-Sculpt® Process. *Physics Procedia*, 12, Part A(0):529–536, 2011.

[26] Xichang Wang, Enming Guo, Shuili Gong, Bruce Dance, Anita Buxton, and Colin Ribton. Application of electron beam surfi-sculpt technology during composites materials joining. *8th International Electron Beam Welding Conference*, 2012.

[27] Chao-Ting Chi, Chuen-Guang Chao, Tzeng-Feng Liu, and Che-Chung Wang. A study of weldability and fracture modes in electron beam weldments of AZ series magnesium alloys. *Materials Science and Engineering: A*, 435–436(0):672–680, 2006.

[28] A Munitz, C Cotler, H Shaham, and G Kohn. Electron beam welding of magnesium AZ91D plates. *Welding Journal - New York*, 79(7):202–s, 2000.

[29] MatWeb Material Property Data. `http://www.matweb.com`, January 2014.

[30] Frank Witte, Jens Fischer, Jens Nellesen, Horst-Artur Crostack, Volker Kaese, Alexander Pisch, Felix Beckmann, and Henning Windhagen. In vitro and in vivo corrosion measurements of magnesium alloys. *Biomaterials*, 27(7):1013–1018, 2006.

[31] Joseph R Davis. *Properties and selection: nonferrous alloys and special-purpose materials*, volume 2. Asm Intl, 1990.

[32] Herbert Wittel, Dieter Muhs, Dieter Jannasch, and Joachim Voßiek. Toleranzen, Passungen, Oberflächenbeschaffenheit. In *Roloff/Matek Maschinenelemente*, pages 21–37. Springer Fachmedien Wiesbaden, 2013.

[33] A Maltais, D Dubé, M Fiset, G Laroche, and S Turgeon. Improvements in the metallography of as-cast AZ91 alloy. *Materials Characterization*, 52(2):103–119, 2004.

[34] Tianping Zhu, Zhan W. Chen, and Wei Gao. Microstructure formation in partially melted zone during gas tungsten arc welding of AZ91 Mg cast alloy. *Materials Characterization*, 59(11):1550–1558, 2008.

[35] SF Su, HK Lin, JC Huang, and NJ Ho. Electron-beam welding behavior in Mg-Al-based alloys. *Metallurgical and Materials Transactions A*, 33(5):1461–1473, 2002.

[36] C-T Chi, C-G Chao, T-F Liu, and C-C Wang. Optimal parameters for low and high voltage electron beam welding of AZ series magnesium alloys and mechanism of weld shape and pore formation. *Science and Technology of Welding & Joining*, 13(2):199–211, 2008.

[37] RG Flemming, CJ Murphy, GA Abrams, SL Goodman, and PF Nealey. Effects of synthetic micro-and nano-structured surfaces on cell behavior. *Biomaterials*, 20(6):573–588, 1999.

Appendix

create_single_figure.m

```
%% CREATE COORDINATE MATRICES FOR EBW FIGURES W/ EQUAL SPACING ------------
% Author: Markus Stuetz, Date: 26.09.2013
% ------------------------------------------------------------------------
%
%% Enter Values for FIGURE

clf; clear;

corners=6;           % Type of polygon (e.g. 6 = hexagon)
arms=30;            % No. of arms of figure

points=300;         % Total coord. points to be calculated?

overlap=0;           % Arm center overlap in %

spiral_angle=0;      % Spiral angle (deg)

equal_spacing=0;     % set 1 for equal point spacing, 2 for custom spacing

% Input END -------------------------------------------------------------

%% Calculate outer contour
arms_per_segment=floor(arms/corners);

arms=arms_per_segment*corners;
angle_inc= 2*pi()/arms;      % in radian

arm_count = 1:arms;
angle = angle_inc * arm_count - angle_inc;

points_per_arm=floor(points/arms);      % 'floor' rounds down
total_points=points_per_arm*arms;       % Actual point output

%% Create spiral values
spiral_angle=spiral_angle *pi()/180;    % in radian

point_count=1:points_per_arm;
spir_inc= spiral_angle/points_per_arm;  % Angle increment

total_increments=2*pi()/spir_inc;       % Amount of increments total

%% Geometric calculation
angle_inner_corner=pi()*(1/2-1/corners);

gamma=pi()-angle_inner_corner-angle(1:arms_per_segment);
sine_aux=sin(gamma).^-1;                          % Inverting elements
length_arm=sin(angle_inner_corner)*sine_aux;

length_arm_all=repmat(length_arm,1,corners);    % Acummulate lengths

x_end=length_arm_all.*cos(angle);   % Contour points
y_end=length_arm_all.*sin(angle);   % --------------

```

```
% theta = angle, z = length_arm_all ... polar coordinates of end points

if equal_spacing==1
        total_length=sum(length_arm_all);
    point_spacing=total_length/points;

    arm_increments_equal = []; angle_equal = []; total_points=0;
    points_per_arm_matrix=[];       % Initialize variables

    for i=1:arms
        current_angle=angle(i);
        j=0;
        while j<=length_arm_all(i)
            arm_increments_equal = [arm_increments_equal j];
            angle_equal= [angle_equal current_angle];
            j=j+point_spacing;
            total_points=total_points+1;
        end
        points_per_arm_matrix=[points_per_arm_matrix int32(j/point_spacing)];
    end
    total_points
    points_per_arm_matrix;
    [x_complete,y_complete]=pol2cart(angle_equal,arm_increments_equal);
elseif equal_spacing==2

else
    arm_increments=(0:points_per_arm-1)/(points_per_arm-1);

    % Create overlap
    overlap=overlap/100;
    arm_increments_shift=arm_increments.*(1+overlap);
    arm_increments_shift=arm_increments_shift-ones(1,points_per_arm)*overlap;

    s_angle_increments=fliplr(arm_increments)*spiral_angle;     % Flip matrix

    s_angle_increments_rep=repmat(s_angle_increments,arms,1);   % repeat rows
    angle_rep=repmat(angle,points_per_arm,1);                   % -----------

    theta_complete=s_angle_increments_rep'+angle_rep;   % Points in polar
    z_complete=arm_increments_shift'*length_arm_all;    % coordinates ---

    [x_complete,y_complete]=pol2cart(theta_complete,z_complete); % Transform
end

hold on;
plot(x_end,y_end,'*-')
plot(x_complete,y_complete,'.-')
%polar(theta_complete,z_complete,'o')
%polar(s_angle_increments,arm_increments)
hold off;
```

create_figure_array.m

```
%% CREATE FIGURE ARRAYS FROM SINGLE FIGURE -------------------------------
% Author: Markus Stuetz, Date: 29.07.2013
% -------------------------------------------------------------------------
%
%% Enter Values for ARRAY
% NOTE: create_single_figure.m has to be run first!

x_number=3;     % How many columns?
y_number=3;     % How many rows?

x_offset=3;         % Offset first to second x-figure in x-direction
y_offset=sqrt(3)/2;       % Offset first to second y-figure in y-direction

x_displacement=1.5;     % Displace rows (usuallay x_offset/2)

filename='show.b01';    % Output file name

% Create picture of array
print_plot=0;   % Set 1 to create .png of plot window
diameter=4;     % Polygon diameter in mm for beam travel calc.
x_array=10;     % Array's x and y latitude for .png print
y_array=6;
x_res=1500;     % X resolution of .png in pixels

% Enter machine specific data
x_machine_max=65535;    % Machine coordinate transformation X,Y
y_machine_max=65535;

% Input END -------------------------------------------------------------

%% Stack figures to create array
% Assume single figure
figures=x_number*y_number;

x_all_coord_sx=x_complete;
y_all_coord_sx=y_complete;

if equal_spacing==1
    % Create x-row: Multiply figure coordinates
    for i=1:x_number-1
        x_all_coord_sx=[x_all_coord_sx;x_complete+x_offset*i];
        y_all_coord_sx=[y_all_coord_sx;y_complete];
    end

    x_all_coord=x_all_coord_sx;     % Prepare acummulated matrices
    y_all_coord=y_all_coord_sx;

    % Create y-rows: Multiply x-row, displace alternatingly
    for j=1:y_number-1
        x_all_coord=[x_all_coord;x_all_coord_sx+x_displacement*mod(j,2)]; % 'mod' gives
             0 or 1 on division by 2, leads to alternation
        y_all_coord=[y_all_coord;y_all_coord_sx+j*y_offset];
    end
else
    % Create x-row: Multiply figure coordinates
    for i=1:x_number-1
        x_all_coord_sx=[x_all_coord_sx,x_complete+x_offset*i];
        y_all_coord_sx=[y_all_coord_sx,y_complete];
    end

    x_all_coord=x_all_coord_sx;     % Prepare acummulated matrices
    y_all_coord=y_all_coord_sx;

    % Create y-rows: Multiply x-row, displace alternatingly
```

```
64      for j=1:y_number-1
65          x_all_coord=[x_all_coord,x_all_coord_sx+x_displacement*mod(j,2)]; % 'mod' gives
                0 or 1 on division by 2, leads to alternation
66          y_all_coord=[y_all_coord,y_all_coord_sx+j*y_offset];
67      end
68  end
69
70  %% Export coordinates for spot figures
71  x_all_base=x_all_coord; y_all_base=y_all_coord;
72
73  %% Transform coordinates into machine coord. system
74  x_dim_max=max(max(x_all_coord));
75  y_dim_max=max(max(y_all_coord));
76  x_dim_min=min(min(x_all_coord));
77  y_dim_min=min(min(y_all_coord));
78
79  x_all_coord_01=(x_all_coord-x_dim_min)/(x_dim_max-x_dim_min); % Shift and normalize to
        interval [0,1]
80  y_all_coord_01=(y_all_coord-y_dim_min)/(y_dim_max-y_dim_min);
81
82  x_all_coord=x_all_coord_01*x_machine_max;  % Adjust X,Y resolution
83  y_all_coord=y_all_coord_01*y_machine_max;
84
85  %plot(x_all_coord,y_all_coord,'.')
86
87  % msgbox('Calculation done, writing file...','Create polygon array','help')
88
89  %% Export to file
90  thefile=fopen(filename,'w');
91
92  if equal_spacing==1
93      % i ... arm no.
94      % k ... figure no.
95      % j ... points of arm i, figure k
96      % m ... go to next arm
97      m=0;
98      %for i=arms:-1:1          % Go from arm to arm (single figure) (clockwise/
            counterclockwise)
99      for i=1:arms
100         for k=1:figures     % Go from figure to figure
101             % Read points of arm (toggle count direction to flip beam movement)
102             for j=points_per_arm_matrix(i):-1:1 % Walls
103             %for j=1:points_per_arm_matrix(i)    % Pins
104                 fprintf(thefile,'%f\t',x_all_coord(k,m+j));   % \t horizontal tab
105                 fprintf(thefile,'%f\n',y_all_coord(k,m+j));   % \n new line
106             end
107         end
108         m=m+points_per_arm_matrix(i);
109     end
110     total_points    % Print total amount of points in command line
111 else
112     %for i=arms:-1:1          % Go from arm to arm (single figure) (clockwise/
            counterclockwise)
113     for i=1:arms
114         for k=1:figures     % Go from figure to figure
115
116             l=arms*k-i+1   % Arm index, omits 'arms' columns, then shift one column to
                    the right
117
118             % Read points of arm (toggle count direction to flip beam movement)
119             %for j=points_per_arm:-1:1 % Walls
120             for j=1:points_per_arm    % Pins
121                 fprintf(thefile,'%f\t',x_all_coord(j,l));   % \t horizontal tab
122                 fprintf(thefile,'%f\n',y_all_coord(j,l));   % \n new line
123             end
124         end
```

```
125     end
126 end
127 fclose(thefile);
128 
129 %% Write information file
130 % Determine beam movement
131 if j==1
132     direction='Wall';
133 else
134     direction='Pin';
135 end
136 
137 fileinfo=strcat(filename,'.info');
138 infofile=fopen(fileinfo,'w');   % Create filename for info-file
139 
140 fprintf(infofile,'INFORMATION FOR %s\r\n', filename); % \r carriage return, for proper
        display in MS notepad
141 fprintf(infofile,'--------------------------------------%s-\r\n', date);
142 fprintf(infofile,'Structure:\t\t%s\r\n',direction);
143 fprintf(infofile,'Polygon type:\t\t%g\r\n',corners);
144 fprintf(infofile,'Arms per figure:\t%g\r\n', arms);
145 fprintf(infofile,'Center overlap:\t\t%g %%\r\n', overlap*100);
146 fprintf(infofile,'Spiral angle:\t\t%g deg\r\n', spiral_angle*180/pi);
147 fprintf(infofile,'Array type (X,Y):\t%g x %g\r\n',x_number,y_number);
148 fprintf(infofile,'Figures total:\t\t%g figures\r\n',figures);
149 fprintf(infofile,'Total points:\t\t%g\r\n', total_points*figures);
150 fprintf(infofile,'Beam travel:\t\t%g mm', sum(length_arm_all)*diameter/2*figures);
151 fprintf(infofile,', for %g mm fig. diam.\r\n', diameter);
152 %fprintf(infofile,
153 
154 fclose(infofile);
155 
156 % msgbox('File written. See *.info for reference.','Create polygon array','help')
157 
158 %% Create figure plot
159 if print_plot==1    % Create image from figure array
160     x_all_coord_mm=x_all_coord_01*x_array;  % Scale to mm
161     y_all_coord_mm=y_all_coord_01*y_array;  % -----------
162 
163     plot(x_all_coord_mm,y_all_coord_mm,'.')
164 
165     axis equal; set(gcf,'PaperPositionMode','auto');    % Set ratio, scale plot
166     set(gcf,'Position',[0 0 x_res/2 y_array/x_array*x_res/2]);
167     axis([(-x_array*.05) (x_array*1.05) (-y_array*.05) (y_array*1.05)]);
168 
169     print('-dpng',strcat(filename,'.png'),'-r200');     % Create .png file
170 else    % Create simple plot
171     plot(x_all_coord,y_all_coord,'.')
172 end
173 
174 %% Export base array for fill array
175     x_base=x_all_coord;y_base=y_all_coord;
```